International Journal of Fatigue 211 (2026) 109723

Contents lists available at ScienceDirect

International Journal of Fatigue

journal homepage: www.elsevier.com/locate/ijfatigue

A novel notch mechanics-based fatigue assessment of additively manufactured lattice structures from aluminium A205☆

Francesco Collini [a], Berk Baris Celik [b], Emilie Beevers [b], Brecht Van Hooreweder [b], Giovanni Meneghetti [a,*]

[a] University of Padova, Department of Industrial Engineering, via Venezia 1, 35131, Padova, Italy
[b] Department of Mechanical Engineering, KU Leuven, Celestijnenlaan 300, Leuven, 3001, Belgium

ARTICLE INFO

Keywords:
Lattice structures
Linear Elastic Fracture Mechanics (LEFM)
Peak Stress Method (PSM)
Additive manufacturing
Selective Laser Melting (SLM)
Laser Powder Bed Fusion (L-PBF)
Averaged Strain Energy Density (SED)
Multiaxial fatigue
Defects
Notches

ABSTRACT

This investigation applies non-conventional extensions of the linear elastic fracture mechanics, known as notch mechanics, for estimating the fatigue limit of Additively Manufactured (AMed) lattice structures. Being based on local stress field analysis, notch mechanics allows the estimation of the fatigue limit of lattice structures by considering them as defective and notched materials and by using a fatigue design tool (the so-called Atzori–Lazzarin–Meneghetti, ALM, diagram) valid for multiaxial local stresses. Theoretical estimations are validated against experimental data coming from two batches of AMed lightweight A205 aluminium alloy lattice structures having Body Centered Cubic (BCC) and diamond Unit Cells (UCs), respectively. The theoretical fatigue limits estimated by using the multiaxial ALM diagram shows errors below 15% compared to the experimental results.

1. Introduction

In the context of the green transition, developing lighter and stiffer novel materials that are yet suitable for manufacturing critically loaded components is a promising prospect. Considering that the transportation industry accounts for about 37% of the total CO_2 emissions in 2017 in the US [1], the development of lighter new materials to reduce weight and thus fuel consumption of vehicles is a crucial step towards a more sustainable future.

For the past decades, the industry of lightweight structures has been dominated by light alloys (such as those based on titanium, aluminium, and magnesium) and composite materials. Periodic lattice structures, are a type of metamaterials that are obtained by the periodic repetition of a Unit Cell (UC) in a 3D design space. As shown in Fig. 1 they allow to fill a portion of the material selection diagram characterized by high stiffness-to-weight ratios, making them competitive with composite materials. During the past two decades, thanks to the development of Additive Manufacturing (AM) technologies, in particular Laser-Powder Bed Fusion (L-PBF), it became possible to obtain low relative density values for small-sized components, and lattice structures have been gaining significant interest from the aerospace, automotive (in particular for motorsport applications) and biomedical industries [2–4].

However, the industrial applications of lattice structures, especially in critically loaded components, have not met the potential of AM lattice structures; one of the most limiting factors is the concerns related to their structural integrity, especially under fatigue loading. These concerns are intrinsically associated with the defects characteristic of AMed materials and the intricate geometry of lattice structures, which together may lead to unsatisfactory fatigue strength and make the fatigue assessment challenging.

There are multiple aspects to address to develop light and fatigue-resistant lattice structures, such as: (i) improving the quality of the AMed lattice structures by optimizing the AM process, (ii) better understanding the fatigue strength of lattice structures, and (iii) optimizing the geometry in view of specific applications for example carrying out multiple functions (e.g., load carrying heat exchangers [2]). The present investigation does not focus on the process parameters or geometric optimization of lattice structures, but on investigating their fatigue damage mechanisms and fatigue limit estimation model.

In general, it is widely acknowledged that the fatigue damaging phenomena are local, and are driven by the irreversible dislocation motion which is favored by stress concentrations such as manufacturing defects (e.g., surface roughness and internal voids) and notches (e.g., the nodes of strut-based lattice structures), [7–9]. Accordingly, the state-of-the-art analysis of notched and defective materials subjected to multiaxial

☆ This article is part of a Special issue entitled: 'FDMD 5' published in International Journal of Fatigue.

* Correspondence to: Department of Industrial Engineering, University of Padova, via Venezia, 1 - 35131 Padova, Italy.
E-mail address: giovanni.meneghetti@unipd.it (G. Meneghetti).

https://doi.org/10.1016/j.ijfatigue.2026.109723
Received 12 February 2026; Received in revised form 17 April 2026; Accepted 1 May 2026
Available online 7 May 2026
0142-1123/© 2026 The Authors. Published by Elsevier Ltd. This is an open access article under the CC BY license (http://creativecommons.org/licenses/by/4.0/).

List of symbols

E	Young's modulus of the base material
ρ	Density of the base material
$\gamma_i, \mathrm{i} = 1,2,3$	Singularity exponent of the stress field ahead of notches and cracks for mode 1,2,3 local stresses, respectively
K_I	Mode I Stress Intensity Factor (SIF)
$K_\mathrm{i}^\mathrm{v}, \mathrm{i} = 1,2,3$	Notch-Stress Intensity Factor (N-SIF) for mode 1,2,3 local stresses, respectively
Δ	Range of a quantity, i.e. algebraic difference between the maximum and minimum values in a load cycle
ΔK_th	Threshold SIF range
$\Delta K_\mathrm{1,th}^\mathrm{v}$	Threshold N-SIF range for mode 1 local stresses
$\Delta K_\mathrm{th,LC}$	Crack propagation threshold for mode I long cracks
$\Delta K_\mathrm{eq\Delta\overline{w},th}^\mathrm{v}$	Threshold range of the equivalent N-SIF for sharp notches subjected to multiaxial loading
K_tg	Elastic stress concentration factor referred to the gross section of the specimen
a	Reference dimension of a crack or notch
α, α_γ	Geometric shape factor for a component containing a crack or a notch, respectively
a_eff	Effective crack size
a_0	El Haddad–Smith–Topper material length parameter
$a_\mathrm{eq\Delta\overline{w}}^\mathrm{v}$	Equivalent effective crack size for local multiaxial stresses
$a_\mathrm{0,eq\Delta\overline{w}}^\mathrm{v}$	Equivalent material length parameter for a V-notched component subjected to multiaxial local stresses
σ_g; σ_ghom	Remote gross nominal stress, homogeneous remote gross nominal stress, respectively
$\Delta\sigma_\mathrm{g}$; $\Delta\sigma_\mathrm{ghom}$	Range of the remote gross nominal stress, range of the homogeneous remote gross nominal stress
$\Delta\sigma_\mathrm{g,th}$; $\Delta\sigma_\mathrm{g,thhom}$	Threshold range of the remote gross nominal stress, threshold range of the homogeneous remote gross nominal stress
$\Delta\sigma_0$, $\Delta\sigma_0\,(R)$	Plain specimen fatigue limit in terms of stress range, stress ratio dependent plain specimen fatigue limit
R_c	Material structural volume radius
$\Delta\overline{w}$	Range of the averaged Strain Energy Density (SED) in the structural volume
$\Delta\overline{w}_\mathrm{th}$	Threshold range of the averaged SED in the material structural volume
HV	Vickers Hardness
N_f	Number of cycles to failure
σ_Y	Yield strength of the material
R	Force ratio or stress ratio, defined as the ratio between the minimum and maximum force or stress in a load cycle

List of acronyms

ALM	Atzori–Lazzarin–Meneghetti
AM	Additive Manufacturing
AMed	Additively Manufactured
LEFM	Linear Elastic Fracture Mechanics
N-SIF	Notch-Stress Intensity Factor
PBF, L-PBF, EB-PBF	Powder Bed Fusion, Laser-PBF, Electron Beam-PBF
PSM	Peak Stress Method
SIF	Stress Intensity Factor
SED	Strain Energy Density
UC	Unit Cell

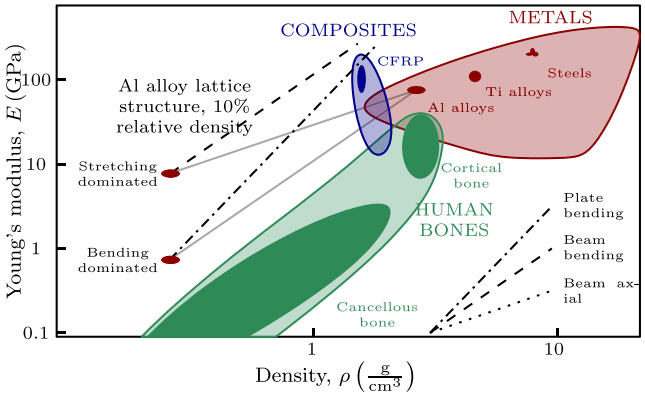

Fig. 1. Materials selection diagram for optimal stiffness-to-weight ratio; the optimal selection curves are reported in the bottom right corner with dotted, dashed, and dash-dotted lines for beams subjected to axial loading, bending loading and plates subjected to bending loading respectively; apparent macroscopic material properties for Al lattice structures schematically estimated using Ashby's equations reported in [5];.
Source: Figure adapted from [6].

fatigue typically consists of a detailed analysis of the local stress field in the vicinity of such features to determine the local fatigue driving force, which is then compared with a fatigue resistance curve that depends on the material, microstructure, and environment. Since the local stress field analysis directly incorporates geometrical effects into the fatigue driving force, there is no need to calibrate component-specific fatigue data. Several local stress field fatigue models are based on Neuber's physical idea, according to which the fatigue strength of a material is governed by stress/strain quantities averaged over a finite volume of material in the proximity of the stress raiser [10]. They allow a unified treatment of defects and notches presenting different size, shape and local stress field. The interested reader is referred to [11–20] for some notable examples.

Local stress field-based approaches are rarely applied to lattice structures; some relevant contributions include: [21–24] where a critical distance approach is adopted using the geometry of the real structure measured with a μX-CT scan; [25] who addressed the low cycle fatigue strength of lattice structures using an averaged Strain Energy Density (SED) based on Ellyn's formulation to account for the significant plasticity characteristic of low cycle fatigue. Due to the high computational cost, time requirements, and complexity of the analysis, designing lattice structures using local stress field approaches on the μX-CT scan geometry is currently challenging for industrial applications, even though the method has shown satisfactory results, while providing access to detailed damage analysis [26], that would otherwise be unattainable without μX-CT scan technologies.

The present analysis adopts the Atzori–Lazzarin–Meneghetti (ALM) diagram. According to its original formulation, it provides a unified fatigue model for cracks, defects, U- and V-shaped notches subjected to local mode 1 stresses, in which geometrical effects in fatigue are accounted for through the evaluation of the local stress field and the

only material parameters required are the plain material fatigue limit, $\Delta\sigma_0$, and the crack propagation threshold for mode I long cracks, $\Delta K_{th,LC}$. In this framework, the local stress field intensities required by the ALM diagram can be evaluated according to the Peak Stress Method (PSM) [27–29], which enables their rapid estimation from linear elastic Finite Element (FE) analyses using relatively coarse meshes and limited post-processing, thereby significantly reducing the overall computational and post processing effort.

Recently, the ALM diagram has been extended to local multiaxial stress fields [30]. The ALM diagram-based fatigue limit estimations proved satisfactory for AMed materials subjected to uniaxial tension loading [6,31–34], and its extension to multiaxial loading was validated against 120+ experimental fatigue limits for defective and sharply notched wrought materials taken from the literature [30].

The challenges to overcome for assessing the validity of the theoretical framework briefly introduced above are the following:

- producing lattice structures with a high-quality finish;
- the development of a testing setup–specimen geometry system that: (i) ensures that the fatigue failure of the lattice structure is properly captured and (ii) allows the observation of the fatigue crack initiation and growth mechanisms;
- the calibration of the base material properties.

In view of that, an extensive experimental analysis was conducted on L-PBFed lattice structures from the aluminium alloy powder A205, which is lightweight and known to result in high strength. In more detail, two series of lattice structures with different UCs, namely the Body Centered Cubic (BCC) and Diamond (D) were tested under axial fatigue loading. To obtain lattice structures with high geometry fidelity the multiple-infill contour printing strategy and optimized process parameters proposed by Beevers et al. [35] were adopted.

This manuscript is organized as follows: Section 2 introduces the theoretical framework to estimate the fatigue limit of lattice structures; Section 3 presents the materials and methods, and the details of the experiments performed to ensure repeatability; Section 4 reports the experimental results; Section 5 discusses the results and compares them with the theoretical fatigue limit estimations according to the ALM model, and then in Section 6 the experimental fatigue limits together with the ALM model fatigue limit estimations are compared to estimations according to the SED model; eventually Section 7 reports the conclusions, highlighting the crucial findings.

2. Theoretical background

This section briefly introduces the theoretical framework proposed in [30] for the multiaxial fatigue assessment of sharply notched and defective metallic materials. It is based on the ALM diagram [36–38] and the averaged SED fatigue model [19], to account for the notch size, acuity, and local multiaxial stress states.

2.1. Stress field analysis of notched geometries, and the ALM diagram: the role of the notch size, acuity and shape

Let us analyze the local stress field in the proximity of a V-notch of size $2a$ and opening angle 2α subjected to pure mode 1 local stresses due to a remote stress σ_g in an infinite plate, as illustrated in Fig. 2; starting from the pointed V-notch condition (i.e., $\rho = 0$, green curve in Fig. 2) two different regions can be identified:

1. the singularity-dominated region with a singularity exponent γ_1 dependent on 2α [39] ($\gamma_1 = 0.5$ for cracks), where, referring to the reference system of Fig. 2, the stress field singularity is uniquely described by the Notch-Stress Intensity Factor (N-SIF) [38,40]:

$$K_1^v = \sqrt{2\pi} \lim_{x\to 0^+,\rho=0} \sigma_{yy} x^{\gamma_1}, \tag{1}$$

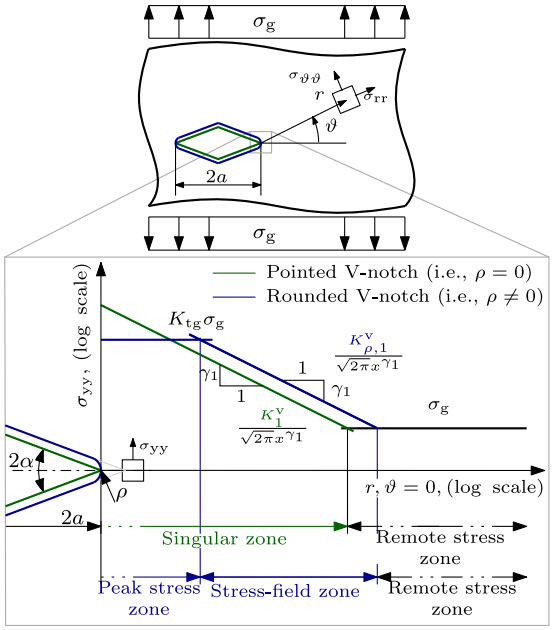

Fig. 2. Schematic stress field of a rounded and pointed V-notch under linear elasticity assumption;.
Source: Adapted from [30].

$$K_1^v = \alpha_{\gamma_1} \sigma_g \sqrt{\pi} a^{\gamma_1} \rightarrow = \sigma_g \sqrt{\pi} a_{eff}^{\gamma_1}, \tag{2}$$

where: α_{γ_1} is a shape factor accounting for the notched component geometry and remote loading condition system; $a_{eff} = \alpha_{\gamma_1}{}^{1/\gamma_1} a$, is the effective crack size;

2. the remote stress zone where the singularity vanishes and approaches asymptotically the remote stress σ_g. In a finite size component, the stress field asymptotically approaches the net stresses acting on the section weakened by the crack/notch.

The two asymptotic stress fields (namely the singular stress field for $x \to 0$ and the uniform remote stress field σ_g for $x \to \infty$) intersect at $a_{eff}/\left(\sqrt{2}\right)^{\frac{1}{\gamma_1}}$, which can be thought of as an estimator of the extension of the singular stress field.

In the case of a rounded V-notch, the stress field does not approach infinity for $x \to 0$, but in the near proximity of the notch tip it is dominated by the theoretical stress concentration factor, K_{tg} [41,42]; however, the stress field is characterized by a severe stress gradient that resembles that of the pointed V-notch and is described by the N-SIF for rounded notches $K^v_{\rho,1}$. Under the approximation $K^v_{\rho,1} = K^v_1$, that holds with sufficient accuracy for sharp notches [42,43], note that the transition from the K_t-dominated region to the stress field-dominated region (from now on called the N-SIF-dominated region) is at the abscissa $a_{eff}/\left(\sqrt{2}K_{tg}\right)^{\frac{1}{\gamma_1}}$, which is exactly $1/K_{tg}^{\left(\frac{1}{\gamma_1}\right)}$ times the extension of the singularity region of the pointed V-notch associated to the rounded V-notch under examination.

As discussed in [43], the stress field of a sharp V-notch (i.e., $\rho \to 0$ — such as weldments, disk–blade joints, and lattice structures nodes, as will be discussed in the present work), can be approximated by that of the pointed V-notch. Consequently, the asymptotic local stress field of sharp V-notches can be uniquely characterized by the N-SIF K^v_1; if only the asymptotic local stress field exists inside the structural volume, then the fatigue limit conditions can be identified by a threshold value of the N-SIF, $\Delta K^v_{1,th}$, [20], which is considered a material–microstructure–environment system and local stress ratio, R, property.

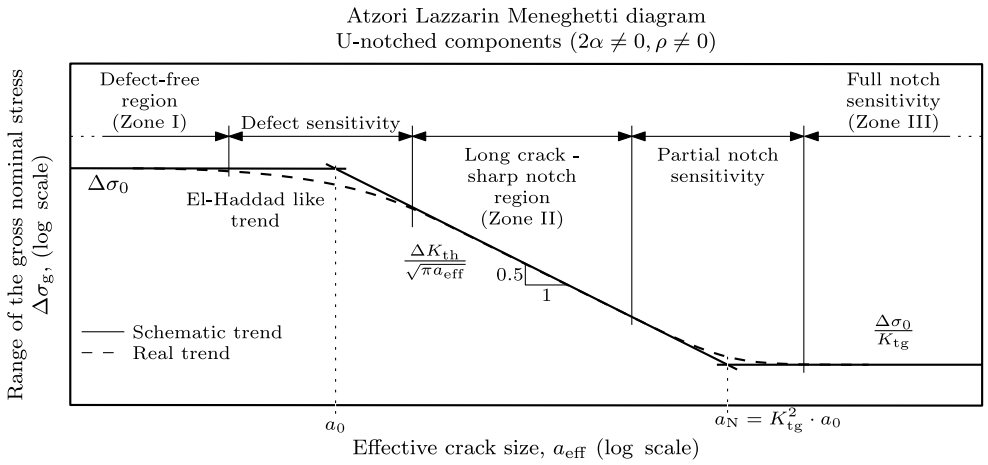

Fig. 3. Schematic ALM diagram formulated for cracks/defects/U-notches [36,37];.
Source: Adapted from [30].

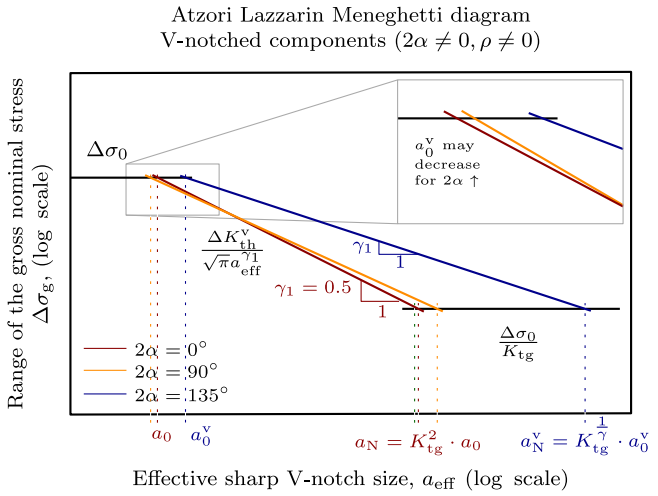

Fig. 4. Schematic ALM diagram extended to V-notches [38];.
Source: Adapted from [30].

Rewriting Eq. (2) in terms of ranges of the stress quantities at the threshold conditions (i.e., $\Delta\sigma_g = \Delta\sigma_{g,th}, \Delta K_I^v = \Delta K_{I,th}^v$), the fatigue limit of a cracked/sharply notched components can be estimated as:

$$\Delta\sigma_{g,th} = \frac{\Delta K_{I,th}^v}{\sqrt{\pi} a_{eff}^{\gamma_1}}, \tag{3}$$

which holds with satisfactory accuracy for long cracks/long and sharp U- and V- notches, but fails to estimate the fatigue thresholds of short cracks/defects (according to Eq. (3) as a_{eff} approaches 0, $\Delta\sigma_{g,th}$ approaches infinity) and that of blunt rounded notches — which, on the other hand, are not relevant for the present study. In the Notch Mechanics framework, the reason why Eq. (3) fails to capture the threshold of short cracks/defects/short V-notches is that additional stress terms come into play inside the structural volume compared to the long crack/long and sharp V-notch case [20].

The relationship between the fatigue strength exhibited by components and changes in (i) notch size, uniquely quantified by a_{eff}, (ii) notch acuity, expressed as a/ρ and quantified by the K_t, and (iii) V-notch opening angle, 2α, can be analyzed by means of the the ALM diagram, for cracks, defects U-notches, and V-notches [36–38]. More specifically, Fig. 3 illustrates the original formulation for cracks, defects and U-notches, whereas Fig. 4, presents the extension to open V-notches. The latter diagram is applicable to the lattice nodes analyzed in the present work, as will be discussed later.

In the ALM diagram (Figs. 3 and 4), the fatigue limit is plotted in terms of the remote nominal stress, $\Delta\sigma_{g,th}$, on the y-axis as a function of the effective crack or notch size, a_{eff}, on the x-axis. It is worth noting that three different regions can be identified: (i) the defect free region, where the fatigue limit approaches the plain material fatigue limit, $\Delta\sigma_0$, (ii) the long crack/long and sharp U- or V-notch region, where the fatigue limit is governed by Eq. (3); (iii) the full notch sensitivity region of blunt notches, where the fatigue limit is governed by the linear elastic peak stress, that is the fatigue limit is estimated as $\Delta\sigma_0/K_{tg}$. These three regions are connected by two transition zones, corresponding to the defect sensitivity and notch sensitivity, respectively.

The transition between the plain material defect-free fatigue limit and the long crack/long sharp V-notch fatigue threshold, can be well described by the ALM model [38] by using an El-Haddad-type correction:

$$\Delta\sigma_{g,th} = \frac{\Delta K_{I,th}^v}{\sqrt{\pi}\left(a_{eff} + a_0^v\right)^{\gamma_1}}, \qquad a_0^v = \left(\frac{1}{\sqrt{\pi}} \frac{\Delta K_{I,th}^v}{\Delta\sigma_0}\right)^{\frac{1}{\gamma_1}}, \tag{4}$$

where a_0^v is the natural extension to open V-notches of the well-known El Haddad–Smith–Topper material length parameter [44,45], as proposed in [38].

Incidentally, the dependence of the fatigue limit on a stress field parameter (i.e. the mode 1 N-SIF, Eq. (3)) makes it clear that the fatigue strength of metallic materials is largely influenced by the stress/strain state existing in a localized, small volume of material, as formerly inferred by Neuber [10,46]. This concept will be taken up again in the next section.

The above mentioned theoretical framework is valid for pure mode 1 local stresses, and therefore does not include the effect of local multiaxial stress fields at notches/cracks/defects. However, in lattice structures, the nodes may be subjected to multiaxial local stress fields, even under uniaxial remote loading conditions.

To address this limitation, the ALM fatigue model was recently extended to include local stress multiaxiality at defects and notches [30]. Such extension exploits the averaged Strain Energy Density (SED) model [19], which is introduced in the next section.

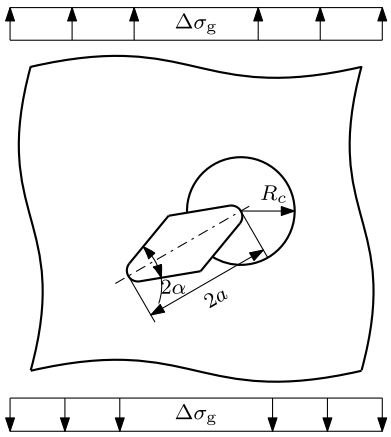

Fig. 5. Averaged SED reference system.

2.2. The averaged Strain Energy Density (SED) model

According to the averaged SED model, the fatigue strength of metallic materials is governed by the averaged SED in a small but finite structural volume [19], $\Delta\overline{w}$. The structural volume is defined as a sector of a cylinder of unit thickness, Fig. 5, and radius R_c, named structural or control radius (note that later formulations include different structural radii for each loading mode).

According to the averaged SED model, the fatigue limit can be uniquely identified by a threshold value $\Delta\overline{w}_{th}$. Both R_c and $\Delta\overline{w}_{th}$ are usually considered material–microstructure–environment system properties, independent of the local stress ratio, R.

The averaged SED in the structural volume of a component weakened by a crack or a pointed (i.e., $\rho = 0$) V-notch subjected to multiaxial local stresses can be computed according to [19] as:

$$\Delta\overline{w} = c_w \sum_{i=1}^{3} \frac{e_i}{E} \left(\frac{\Delta K_i^v}{R_c^{\gamma_i}} \right)^2, \tag{5}$$

where: c_w is a parameter accounting for the local stress ratio R, defined as:

$$c_w(R) = \begin{cases} \dfrac{1+R^2}{(1-R)^2}, & -1 \le R \le 0 \\ \dfrac{1-R^2}{(1-R)^2}, & 0 \le R < 1 \end{cases}; \tag{6}$$

E is the Young's modulus of the base material; $e_i, i = 1,2,3$ are dimensionless coefficients associated with mode 1,2,3 local stresses, respectively, and dependent on the V-notch opening angle 2α and the Poisson's ratio of the base material ν [47]. A more general formulation considers different structural radii for each local stress mode [48], as experimental data show that the structural radius of mode 3 local stresses is usually larger than mode 1 local stresses [30,49].

In order to calibrate the size of the structural volume R_c in Eq. (5), the averaged SED evaluated at the fatigue limit condition of two different specimens' geometries must be considered; usually, the plain specimen and a pointed V-notch (the long crack case being also a valid choice) are considered.

2.3. The ALM diagram for local multiaxial stresses

Referring to Fig. 5, consider a generic V-notch subjected to a remote uniaxial stress field that induces a local multiaxial stress field, as is the case of lattice structures subjected to remote uniaxial loading. The fatigue limit expressed in terms of the remote stress $\Delta\sigma_{g,th}$ can be computed by particularizing Eq. (5) at the threshold condition (i.e., $\Delta\overline{w} = \Delta\overline{w}_{th}$, $\Delta\sigma_g = \Delta\sigma_{g,th}$) and making use of Eq. (2) [30]:

$$\Delta\sigma_{g,th} = \frac{\Delta K^v_{eq\Delta\overline{w},th}}{\sqrt{\pi \left(a^v_{eq\Delta\overline{w}} + a^v_{0,eq\Delta\overline{w}} \right)}}, \tag{7}$$

$$\Delta K^v_{eq\Delta\overline{w},th} = \frac{\sqrt{E\Delta\overline{w}_{th}} \prod_{i=1}^{3} R_c^{\gamma_i}}{\sqrt{c_w}}, \tag{8}$$

$$a^v_{eq\Delta\overline{w}} = \sum_{j=1}^{3} \left(\prod_{i=1}^{3} R_c^{2(1-\delta_{j,i})\gamma_i} \right) e_j a_{eff,j}^{2\gamma_j}, \tag{9}$$

$$a^v_{0,eq\Delta\overline{w}} = \frac{1}{\pi} \left(\frac{\Delta K^v_{eq\Delta\overline{w},th}}{\Delta\sigma_0} \right)^2. \tag{10}$$

If one of the local stress modes is inactive, then the corresponding quantities should be removed from Eqs. (8)–(9). The interested reader is referred to [30] for all the details of the analytical derivation and validation of Eqs. (7)–(10) against 120+ experimental multiaxial fatigue limits from wrought specimens weakened by sharp V-notches and artificial defects. It is worth mentioning that in the previous investigation [30], Eqs. (7)–(10) are formulated, including different structural radii for each local stress mode.

2.4. Calibration of material properties

The calibration of the material properties required for the application of the averaged SED model, can be performed by estimating $\Delta\overline{w}_{th}$ from the fatigue limit of the plain defect-free material, $\Delta\sigma_0$, and then estimating R_c from the long crack fatigue propagation threshold, $\Delta K_{th,LC}$ as:

$$\Delta\overline{w}_{th} = c_w \frac{\Delta\sigma_0^2}{2E}, \tag{11}$$

$$R_c = c_w \frac{e_1}{E} \frac{\Delta K_{th,LC}{}^2}{\Delta\overline{w}_{th}}. \tag{12}$$

In the present analysis, $\Delta K_{th,LC}$ was measured experimentally at $R = 0.1$ according to ISO 12108. The plain material, defect-free fatigue limit $\Delta\sigma_0$ cannot be determined experimentally considering the typical defectiveness of AMed materials; therefore it is necessary to proceed with indirect methods. For lightweight aluminium alloys $\Delta\sigma_0$ can be estimated at $R = -1$ from the ultimate tensile strength of the base material, σ_{UTS}, as follows [50]:

$$\Delta\sigma_0 = m \cdot \sigma_{UTS}, \tag{13}$$

where the calibration constant m ranges from 0.8 to 1 as documented in [50] for several lightweight Al alloy including 1000, 2000, 3000, 5000, 6000, 7000 series. In the context of the present work the calibration constant was assumed to be 1. To account for the influence of the stress ratio, R, the Goodman–Smith equation is used [51] with $m = 1$:

$$\Delta\sigma_0(R) = 2 \left(\frac{1-R}{3-R} \right) \sigma_{UTS}. \tag{14}$$

It should be noted that the estimation error associated with the material parameter $\Delta\sigma_0$ affects the fatigue limit estimation according to Eqs. (7)–(10) to varying degrees, depending on the ratio $a^v_{eq\Delta\overline{w}}/a^v_{0,eq\Delta\overline{w}}$. For low values of this ratio (i.e., short cracks), the influence is significant, whereas for larger values (i.e., long cracks or long, sharp V-notches), its effect becomes negligible.

3. Materials and methods

The experimental analysis was divided into two steps: (i) the estimation of the material properties $\Delta K_{th,LC}$ and $\Delta\sigma_0$ required to calibrate the ALM and SED models, Eqs. (7) and (12); (ii) the validation of the ALM model for fatigue limit estimation.

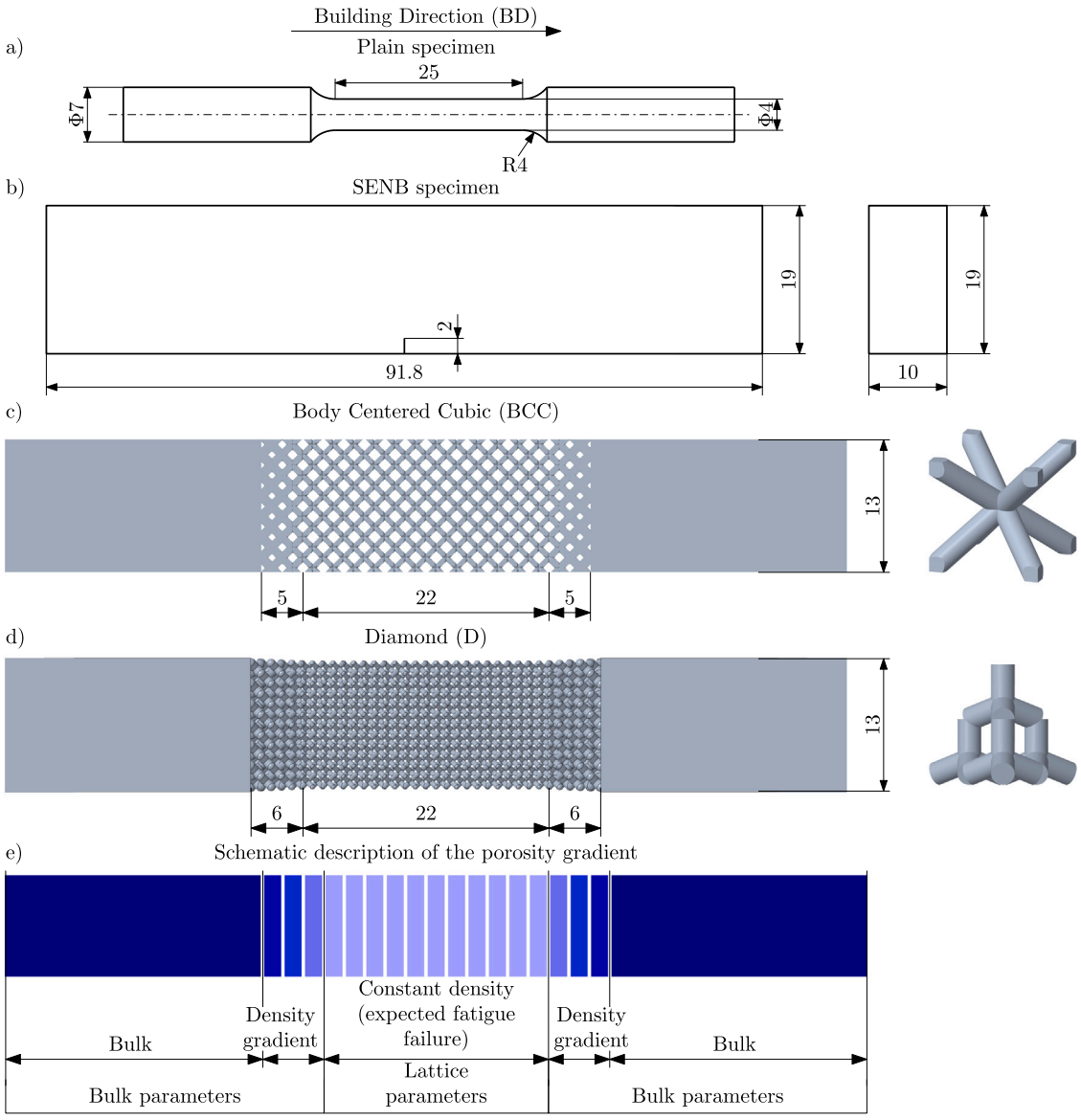

Fig. 6. Specimen geometry; (a) plain specimens; (b) SENB specimens according to ISO 12108 standard; (c) BCC lattice specimens; (d) diamond lattice specimens; (e) schematic description of the partition for lattice structures in bulk and lattice portions; further details on the bulk parameters and lattice parameters in Table 2, Fig. 7.

Table 1
Chemical composition of the A205 alloy from the manufacturer datasheet [52].

Element	Al	Cu	Mg	Ag	Ti	B	Si	Fe
max Wt %	Bal.	5.0	0.33	0.9	3.85	1.55	0.1	0.08
min Wt %		4.2	0.20	0.6	3.0	1.25		

3.1. Manufacturing and specimen geometry

Four different specimens' geometries were analyzed in this study:

1. plain specimens, Fig. 6(a), to (i) characterize the base material from quasi-static tensile tests, (ii) indirectly estimate $\Delta\sigma_0$ using Eq. (14), and (iii) $\Delta\overline{w}_{th}$ using Eq. (11);
2. Single Edge Notch Bending (SENB) specimens, Fig. 6 b), to (i) determine $\Delta K_{th,LC}$ by means of Fatigue Crack Growth (FCG) tests according to ISO 12108 standard, and eventually (ii) calibrate the structural radius R_c using Eq. (12);
3, 4. lattice structures with the BCC, or "star", UC, Fig. 6(c), and lattice structures with the Diamond (D) UC Fig. 6(d), to investigate the fatigue behavior of lattice structures and the notch–defect competition.

The lattice samples present three different regions, as depicted in Fig. 6: (i) a nominally fully dense region at the grip section to ensure that the sample could be fixed to the testing equipment, (ii) the test section, where the relative density is constant and fatigue failure is expected, and (iii) a transition region, where the relative density smoothly changes from the fully dense grip section to the constant relative density of the test section, to avoid fatigue failure initiating at the interface between the test section and the grip section. In the transition region, which extends over three rows of UCs, each strut is modeled as a frustum of a cone, with the diameter varying linearly from the maximum nominal value of a 1 mm at the intersection with the grip section to the nominal value of 0.5 mm in the test section. The UC size was $2 \times 2 \times 2$ mm^3, and the nominal strut diameter was 0.5 mm in the test section for both UCs. Furthermore, a small sample of both UCs was built with the nominal relative density of the test section to measure the

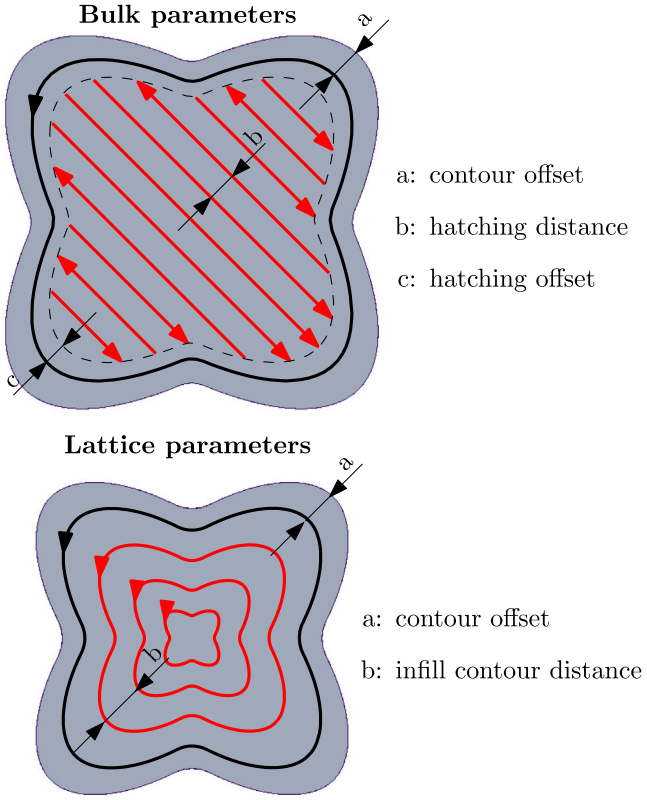

Fig. 7. Schematic description of the laser parameters chosen for the lattice structures manufacturing, further details are provided in Table 2 and Ref. [35].

Table 2
Summary of the process parameters; see Fig. 7 for the physical implication of the scanning parameters.

	Details
Lattice parameters	
Scanning strategy	"Lattice parameters" in Fig. 7
Laser power	130 W
Scanning speed	900 mm/s
Contour offset	80 µm
Infill contour distance	80 µm
Layer thickness	30 µm
Bulk parameters	
Scanning strategy	"Bulk parameters" in Fig. 7
Laser power	263 W
Scanning speed	1250 mm/s
Contour offset	50 µm
Hatching distance	100 µm
Hatching offset	100 µm
Layer thickness	30 µm

manufactured relative density and reproduce it in the Finite Element (FE) models.

All specimens were produced by AM with the L-PBF machine 3D Systems ProX® DMP 320 from A205 powder (see Table 1 for the chemical composition) with the samples standing vertically in the building plate [35].

Referring to Table 2 and Fig. 7, the plain and SENB specimens were printed using process parameters hereafter denoted as bulk. Instead the lattice structures were manufactured adopting two different strategies: the test section (with a nominal strut diameter of $d = 0.5, \text{mm}$) was printed using process parameters hereafter denoted as lattice, whereas the fully dense grip section and the density gradient region of the lattice structure (where $d > 0.5, \text{mm}$) were printed using the bulk parameters. The grip section of the lattice specimens, as well as the fully dense plain and SENB specimens, were printed using a single scanning island.

The lattice structures and the plain specimens were printed in net shape and were tested with surfaces in as-built conditions. The SENB specimens were printed as parallelepipeds with an allowance of 1 mm on each side.

All specimens were cut off the build plate by a wire electric discharge machine with a wire diameter of 0.3 mm. The cleaning process involved standard dismounting practices while removing as much powder as possible, followed by vacuum cleaning and ultrasonic cleaning in ethanol for 30 to 45 min at 40 kHz at nominal room temperature.

The final net geometry of the SENB samples was obtained through machining. At the end of the machining process, the notch was cut by a wire electric discharge machine with a wire diameter of 0.3 mm.

Before mechanical testing all specimens underwent stress relief heat treatment to reduce residual stresses induced by the AM process and, limited to the SENB samples, by the machining process. The stress relief treatment was performed at 270°C for 2 h under inert argon gas, followed by slow furnace cooling. The stress relief heat treatment was not intended to enhance mechanical properties, but solely to eliminate residual stresses. This choice was made to guarantee that the applied force ratio in fatigue tests coincides with the local stress ratio. A conventional T6 heat treatment, which is recommended in the powder manufacturer's datasheet to enhance mechanical properties [52], was intentionally not applied. As reported by Maamoun et al. [53] for AMed AlSi10Mg, the T6 heat treatment does not guarantee complete residual stress relief. While the solution treatment stage likely relaxes manufacturing-induced residual stresses due to the high temperature of the hold stage (not specified in [52], but usually above 500°C), significant residual stresses may be reintroduced during the rapid quenching step. The subsequent artificial aging treatment is typically performed at temperatures insufficiently high to relieve the residual stresses introduced during quenching. Since a similar behavior was expected for the A205 alloy, the aforementioned stress relief heat treatment was preferred.

3.2. Metallurgical characterization

After the mechanical testing, one sample for microhardness measurements and microstructural analysis was extracted from the extremities of the SENB specimens (where the applied stresses had been negligible during fatigue testing) by saw-cutting. The sample preparation involved the following steps:

- grinding with sandpaper of grit P120 up to P1200 and then polishing with 6 µm, 3 µm, and 1 µm diamond suspensions;
- only for the microstructural analysis, the surface of the sample was etched by chemical etching using a solution of 30% water, 10% hydrofluoric acid, 60% hydrogen peroxide for a few seconds before diluting in water.

Vickers microhardness HV was measured using a Shimadzu durometer equipped with a mass of 100 g and a light microscope to measure the indentation size; for the microstructural analysis, a Scanning Electron Microscope (SEM) Zeiss evo MA10 was used.

The relative density was measured with the Archimedes method in an Ohanus balance by measuring the weight of the specimen in air and immersed in ethanol, assuming a density of 2800 $\frac{\text{kg}}{\text{m}^3}$.

3.3. Mechanical testing

3.3.1. Fully dense plain and SENB specimens

Quasi-static tensile tests were performed on five plain specimens using an Instron 3366 machine equipped with an Instron AVE 2 Non-Contacting Video Extensometer.

Fatigue Crack Growth (FCG) tests were conducted according to ISO 12108 under three-point bending in air, at room temperature, with a

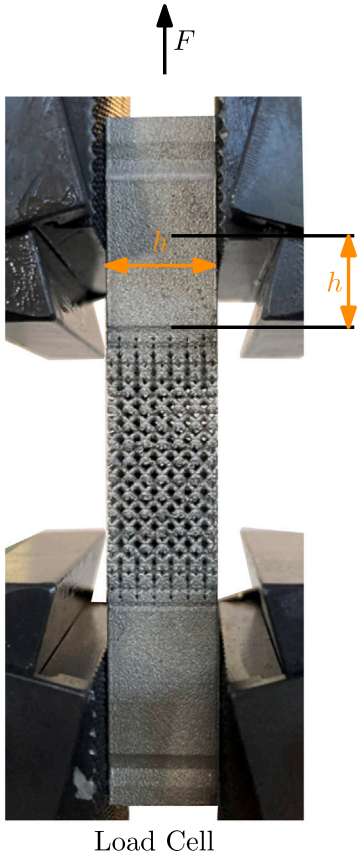

Fig. 8. Schematic representation of the experimental setup for the lattice structures, valid for both BCC and D lattice samples analyzed.

stress ratio $R = 0.1$ and a frequency of $f = 30\,\text{Hz}$, using an in-house experimental setup compliant with the requirements of ISO 12108. The testing machine was a closed loop-controlled STEPLab EA05 electromechanical machine. The crack advance was measured with digital light DinoLite EDGE 5MPx microscopes installed on both sides of the crack; the crack length was measured, stopping the test under force control at maximum crack opening. The Dino-Lite Edge 5 MPx microscopes were calibrated prior to testing using the manufacturer's calibration target.

The pre-cracking was performed with an initial $\Delta K = 5.3\ \text{MPa}\sqrt{\text{m}}$ until a fatigue crack of at least 1 mm was measured, under remote loading with a constant range of $\Delta F = 2120$ N. Then, the stepped force reduction method was applied to execute a K-decreasing test and achieve the threshold conditions, with a normalized K-gradient $c = -0.1\ \text{mm}^{-1}$, starting from the $K_{\max}$ obtained at the end of the pre-cracking. The stepped force reduction was applied after measuring a crack advance of at least 0.5 mm; the reported $\text{d}a/\text{d}N$ was computed by dividing the total crack advance Δa, and the number of cycles ΔN elapsed at constant remote force range.

3.3.2. Lattice samples

All tests were performed at room temperature in air using an Instron ELECTROPULS® E10000 all-electric machine under remote tension loading as illustrated in Fig. 8. The specimen was clamped at a distance at least larger than the specimen thickness h to ensure minimal influence from the clamping system on the stress field in the net section of the specimen.

Quasi-static tensile tests were performed on two specimens for the BCC, and three for D; these tests aimed to evaluate whether fatigue tests in high cycle fatigue were in the linear elastic regime, and thus, if the LEFM assumption is reasonable.

Table 3
Summary of the metallurgical properties of the A205 material.

	Value
Vickers hardness	65 $HV_{0.1}$
Relative density	99.8%

Table 4
Summary of the quasi-static tensile tests results performed on plain specimens.

	Value	min	max
Young's modulus, E (GPa)	72		
Tensile strength, σ_{UTS} (MPa)	250	236.6	259.0
0.2% offset yield strength, σ_{Y} (MPa)	135	126.4	147.1
Elongation at fracture, ε_{f} (%)	18	16.1	20.4

Fatigue tests were performed on 10 BCC samples and 10 D samples; all tests were performed with a loading frequency of 30 Hz under a remote force ratio of $R = 0.1$; the failure criterion is complete specimen separation. The fatigue limit (in terms of the range of the remote nominal stresses referred to the gross section) was identified using the Dixon-modified up-and-down method [54] for each series of tests with short staircase procedures with Run-Out (R-O) at 10^7 cycles; the specific number of samples used in the staircase sequence is reported in Section 4.

4. Results

In this section the results of the experiments described in Section 3 are reported. Results for the lattice structures are reported in terms of the stress in the equivalent homogeneous material associated with the lattice structure at the macroscopic apparent scale, $\sigma_{\text{g,hom}}$, defined as:

$$\sigma_{\text{g,hom}} = \frac{F}{A}, \quad A = h^2, \tag{15}$$

where h and F are quoted in Fig. 8.

4.1. Metallographic characterization

Fig. 9 shows the microstructure, which is characterized by a cellular morphology, with an Al matrix, which appears in a lighter contrast, while thin layers of darker precipitates are observed along the cellular boundaries. In addition, coarsely dispersed precipitates in a brighter contrast are visible in the higher-magnification micrographs shown in Fig. 9(c,d); these are likely titanium diborides characteristic of the A205 alloy, (e.g., [35,52]). Table 3 reports the HV and the relative density of the fully dense material. The soft microstructure, and the grossly dispersed precipitates are symptoms of the overaging that occurred during the stress relief heat treatment.

4.2. Mechanical testing

4.2.1. Fully dense plain and SENB specimens

Fig. 10 and Table 4 report the results of the quasi-static tensile tests conducted on the plain specimens, Fig. 6(a), to characterize the base material properties.

Fig. 11 reports the results of the fatigue crack growth tests conducted on the SENB specimens and the Paris curve fitted on experimental data points considering only data where the fatigue crack growth rate is higher than $10^{-10}\ \frac{\text{m}}{\text{cycle}}$. The threshold value $\Delta K_{\text{th,LC}}$ is defined as the value of ΔK associated to the smallest $\text{d}a/\text{d}N$ measured, which is lower than $10^{-10}\ \frac{\text{m}}{\text{cycle}}$.

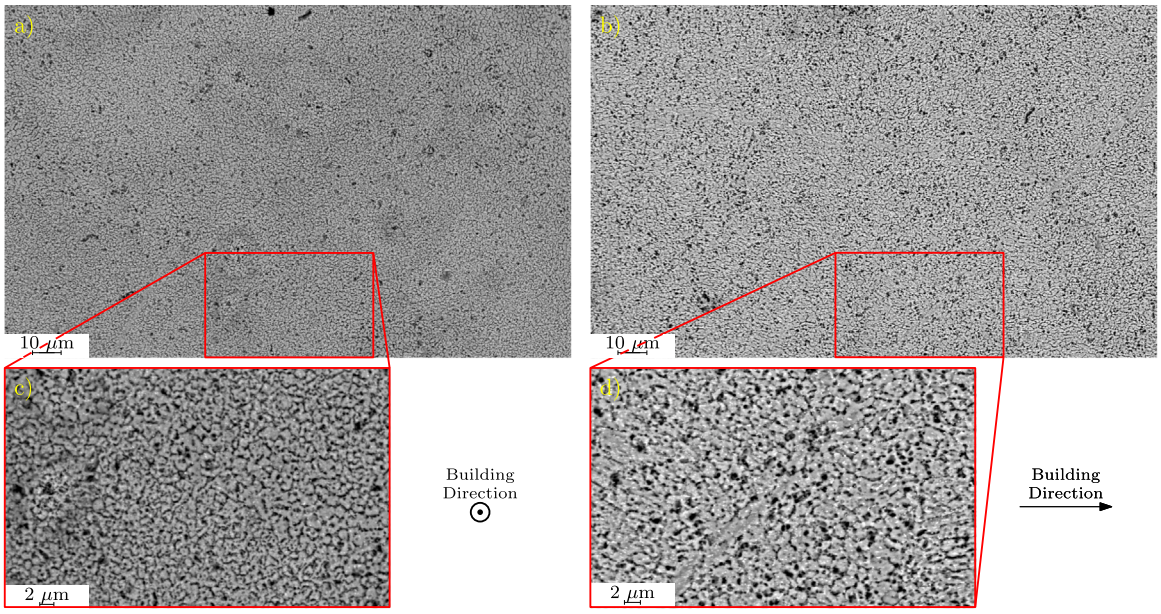

Fig. 9. SEM micrographs of the microstructure obtained after stress relief heat treatment; (a,c) perpendicular to the building direction; (b,d) parallel to the building direction.

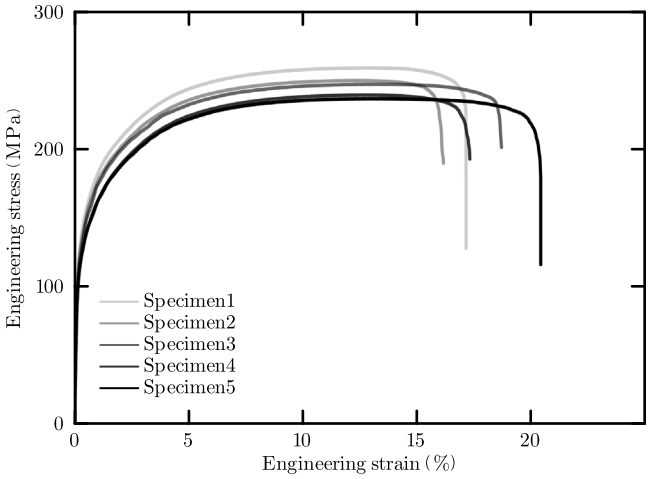

Fig. 10. Engineering stress–strain curve of the quasi-static tensile tests conducted on the base material.

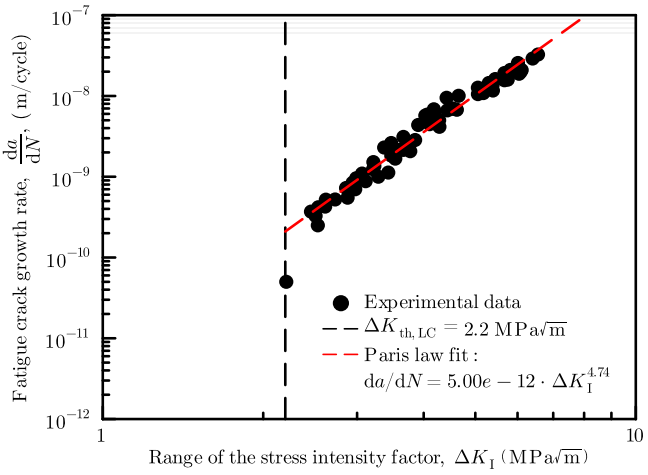

Fig. 11. Fatigue crack growth rate as a function of the stress intensity factor range.

4.2.2. Lattice samples

Figs. 12 and 13 show the results of the quasi-static tensile tests performed on the lattice specimens, Fig. 6(c,d), where the x-axis reports the crosshead displacement of the testing machine. Figs. 14 and 15 report the experimental $\Delta\sigma_{g,hom} - N_f$ curves fitted on the results obtained from fatigue tests on the lattice specimens, Fig. 6(c,d). Each figure includes:

- the experimental data, where failed specimens are indicated by diamond markers, and run-out specimens are indicated by circular markers. The same number reported near some markers indicates a specimen which was re-tested at a higher applied stress level after a run-out test;
- the fatigue limit $\Delta\sigma_{g,th}$ estimated with the Dixon-modified up-and-down method [54], indicated by the horizontal dashed line and the staircase of applied stress levels, where "X" indicates a failed specimen and "O" indicates a run-out specimen;
- the Woehler curve fitting the experimental data (excluding re-tests from the fit), the T_σ for the relevant survival probability (PS) value and a confidence level of 90%; the experimental data are assumed to have a Lieberman k-distribution according to ISO 12107 standard.

5. Analysis of the experimental results and validation of the multiaxial ALM model

This section discusses the experimental results reported in the previous section and compares them with the theoretical fatigue limit estimations according to the ALM model presented in Section 2.

5.1. Analysis of the experimental results

First of all, it should be noted that the fully dense specimens (i.e., plain and SENB samples) and lattice structures were manufactured using different nominal process parameters, which may have led to different microstructures in as-built conditions. However, all

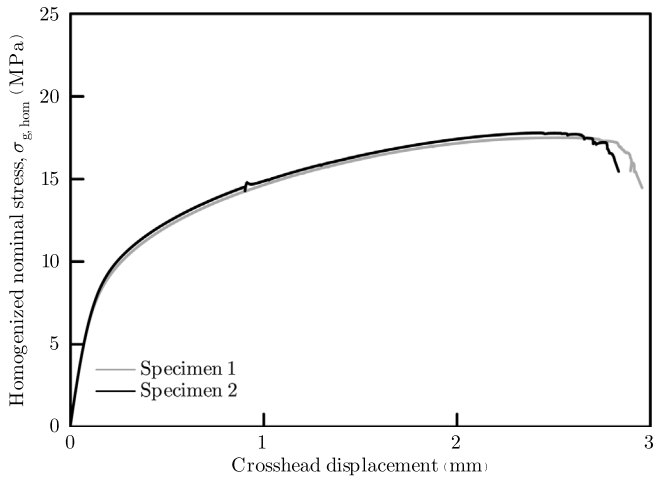

Fig. 12. Engineering stress-crosshead displacement curve of the quasi-static tensile tests conducted on BCC samples.

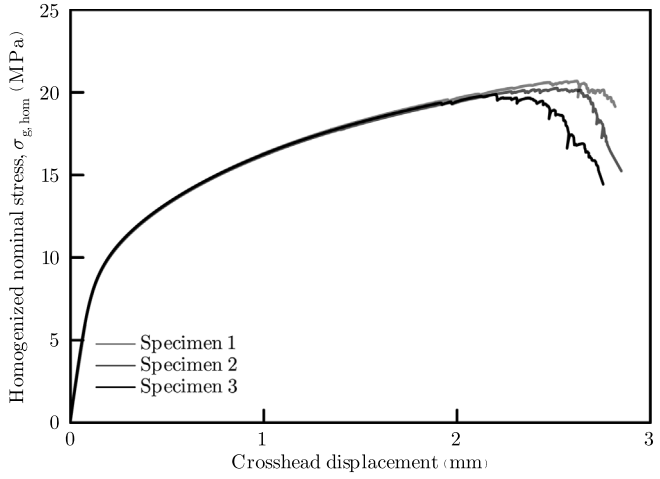

Fig. 13. Engineering stress-crosshead displacement curve of the quasi-static tensile tests conducted on D samples.

samples underwent a post-processing heat treatment leading to an over-aged condition, which is expected to substantially homogenize the microstructure and reduce the differences induced by the manufacturing process in the as-built state. Moreover, it is worth noting that, due to the much smaller characteristic dimensions of lattice structures, (i) the surface-to-volume ratio is much higher, and (ii) the contour scanning affects a larger portion of the scanned section, resulting in a different thermal history during fabrication compared with bulk material. Consequently, even when identical nominal printing parameters are used, bulk and lattice components still experience different cooling conditions and are therefore likely to develop distinct as-built microstructures.

A comparison, in terms of homogenized stresses at the apparent macroscopic scale, between the quasi-static tensile test results for the BCC and D lattices (Figs. 12 and 13) and the corresponding fatigue test results (Figs. 14 and 15) shows that the stress levels applied close to the fatigue limit fall well within the linear elastic regime of the lattice structures. Therefore, the use of a linear elastic approach for the subsequent stress field analysis is justified, since local plasticization at the strut junctions is expected to be limited.

Another conclusion that can be drawn is related to the reduced scatter of the fatigue test results exhibited by both lattice structures, according to the reduced T_σ values obtained from the statistical analysis

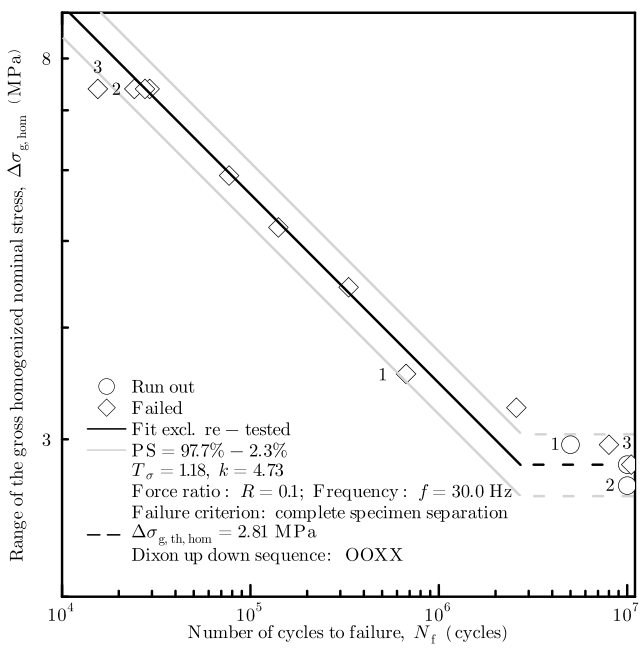

Fig. 14. $\Delta\sigma_{g,hom} - N_f$ curve of the BCC specimens.

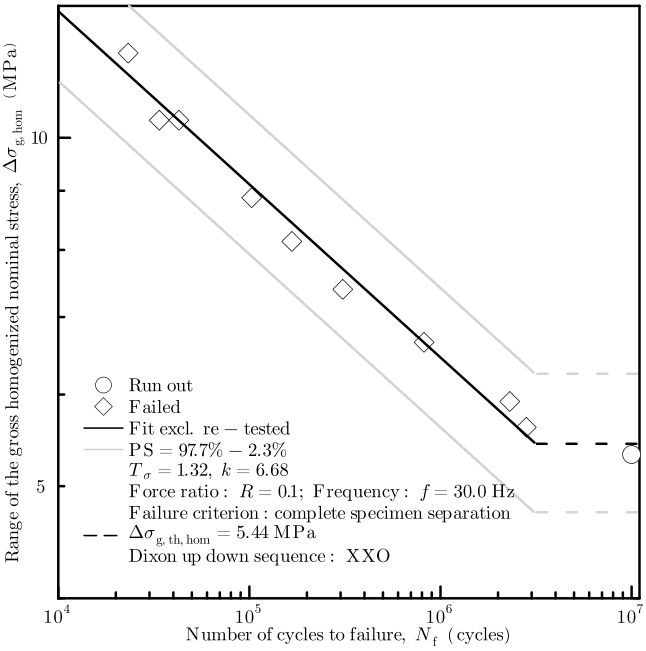

Fig. 15. $\Delta\sigma_{g,hom} - N_f$ curve of the D specimens.

and reported in Figs. 14 and 15. While in AMed plain specimens the statistical distribution of defect size translates into relatively high scatter of fatigue test results, if compared to conventional wrought metallic materials, in the presence of sharp notches, the influence of AM defects becomes negligible [34], owing to (i) the high quality of the samples printed and (ii) the overwhelming detrimental effect of the stress concentration factor introduced by the notch. In the present case, the reduced scatter of fatigue test results suggests that lattice nodes behave like sharp notches, which trigger fatigue crack initiation and homogenize the overall fatigue behavior of the lattice structures.

While the experimental campaign comprised a limited number of specimens, the scatter bands were determined in accordance with the

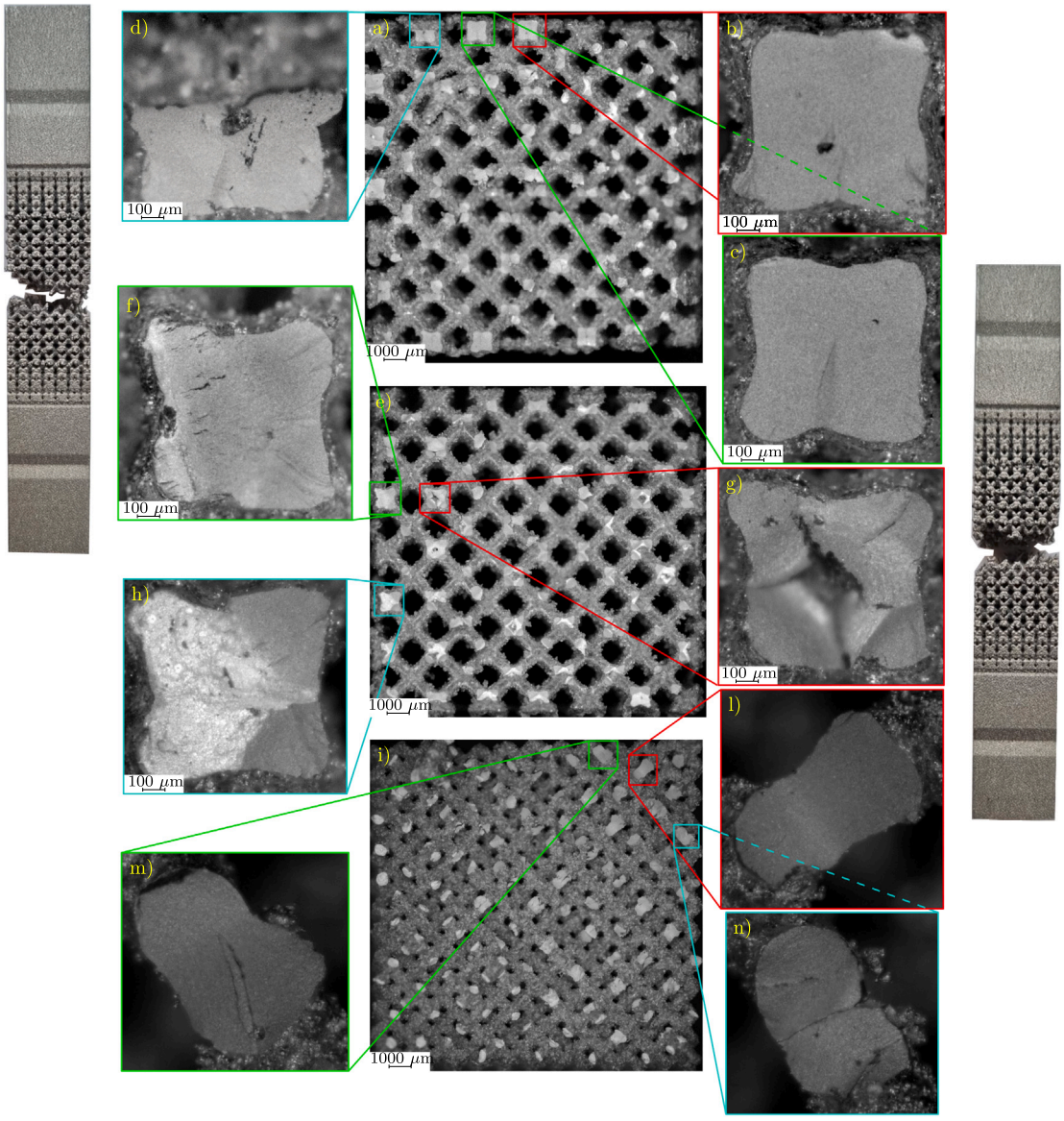

Fig. 16. Fracture surface of the AMed lattice specimens; (a–d) BCC sample tested at $\Delta\sigma_{g,hom} = 2.96$ MPa failed at $N_f = 7.81E6$ cycles; (e–h) BCC sample tested at $\Delta\sigma_{g,hom} = 5.21$ MPa failed at $N_f = 3.33 \cdot 10^5$ cycles; (i–m) D sample tested at $\Delta\sigma_{g,hom} = 5.62$ failed at $N_f = 2.81 \cdot 10^6$ cycles; in subfigures (l–m), no scale bar is shown because the images are composites of multiple focal planes acquired by stereo microscopy, making a unique scale inapplicable. To provide a qualitative indication of the size of the depicted fracture surfaces, the diameter of the struts is approximately 0.52 mm. Side view of the failed specimen highlighting failure location within the constant density region.

statistical procedures defined in ISO 12107. This standard accounts for the uncertainty associated with small sample sizes by employing the Lieberman k-factor to calculate one-sided tolerance limits. An increase in sample size leads to a reduction in the k-factor and, ultimately, to a narrowing of the scatter bands, further highlighting the low intrinsic scatter in the fatigue behavior of the limited number of lattice structures investigated in the present study.

The sharp notch behavior of lattice nodes is further confirmed at the scale of individual UCs. The fracture surfaces observed after fatigue tests are reported in Fig. 16 for both BCC and D UCs, and reveal that internal porosities, incidentally small and rare, do not act as Fatigue Crack Initiation Sites (FCIS). Instead, multiple cracks initiate at the sharp notches of the lattice nodes, both in medium- (Fig. 16(e–g)) and high-cycle (Fig. 16(a–d, i–m)) fatigue regimes. Fig. 16 clearly reveals the sharp notch behavior, where multiple fatigue cracks initiate simultaneously along the entire notch tip line and then coalesce during fatigue crack growth. In contrast, AMed blunt notches (or plain specimens) typically exhibit a single FCIS due to a defect or a deep valley of the surface roughness profile.

Lastly, the fracture surfaces shown in Fig. 16 further reveal that little to no unstable crack propagation occurred in some lattice nodes (e.g., Fig. 16(b,c,f)). This observation indicates that, during stable crack propagation within individual lattice nodes, the remotely applied load is progressively redistributed to other undamaged or less-damaged UCs. In contrast, nearby lattice nodes (e.g., Fig. 16(d,g,h)) exhibit rougher and non-planar fracture surface regions indicating unstable crack propagation.

The effectiveness of the specimen design in ensuring failure within the lattice test section was confirmed by experimental observations. As shown in Fig. 16, the side views of the failed specimens indicate that fracture occurred within the region of constant relative density, away from both the transition zones and the fully dense grip sections.

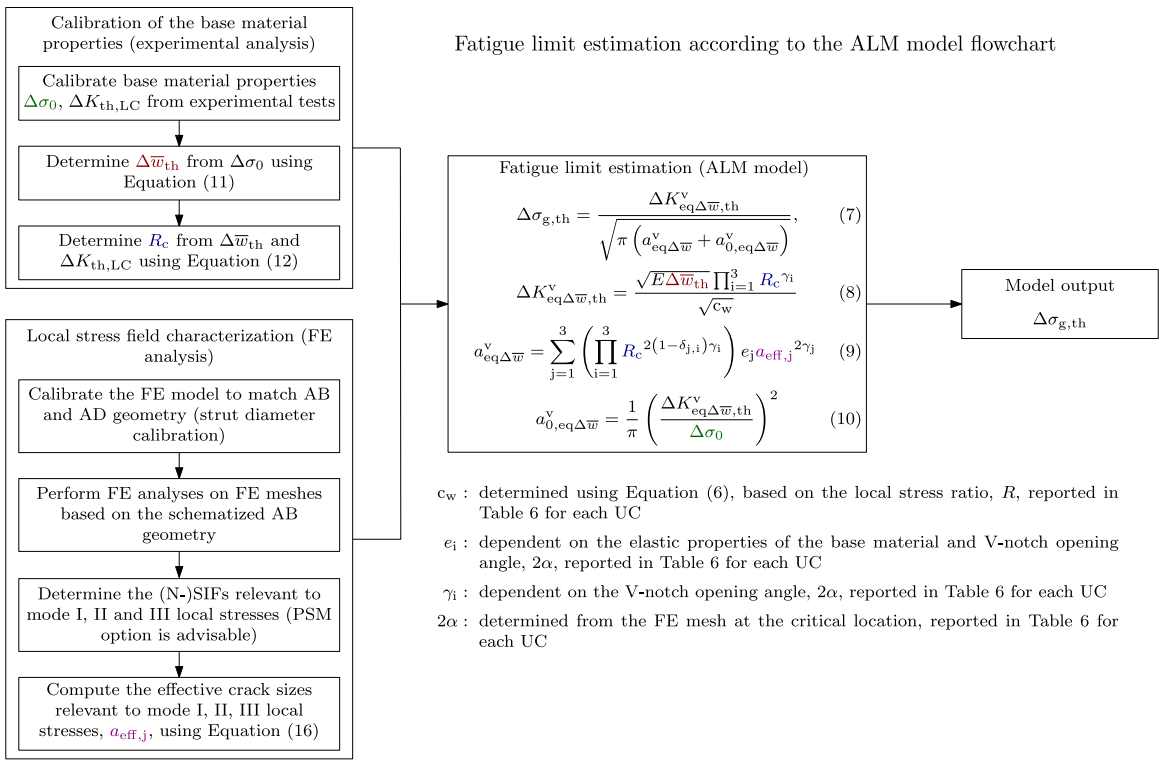

Fig. 17. Schematic flow chart of the procedure adopted to estimate the fatigue limit of lattice structures using the multiaxial ALM framework.

5.2. Validation of the multiaxial ALM model

Based on the observations from the $\sigma - N_f$ curves and the fracture surfaces reported above, it is reasonable to assume that the analyzed lattice nodes behaved as sharp notches, which always triggered fatigue failure. Therefore, the fatigue limit can be estimated using the V-notch theory summarized in the theoretical framework reported in previous Section 2, as summarized in the flow chart of Fig. 17.

To apply Eqs. (7)–(10), the following parameters are required:

- the material properties R_c, and $\Delta\overline{w}_{th}$, which were estimated using Eqs. (11)–(14) fed with the experimental results generated in the present investigation, according to the summary reported in Table 5;
- the linear elastic structure (or notch) properties $a_{eff,i}$, for each relevant loading mode, which were estimated using Eq. (2) as:

$$a_{eff,i} = \left(\frac{K^{v}_{i}}{\sigma_g\sqrt{\pi}}\right)^{\frac{1}{\gamma_1}}, i = 1, 2, 3. \quad (16)$$

where K^{v}_{i} is the N-SIF relevant to the ith local stress mode, determined from FE simulations on the lattice structures employing the Peak Stress Method (PSM) to simplify the numerical analysis. The interested reader is referred to [27,28] for the theoretical framework of the PSM, which is a numerical procedure that allows estimating the N-SIFs using relatively coarse FE mesh patterns, while avoiding the asymptotic analysis of the singular stress field according to Eq. (1); σ_g is the reference nominal stress, which was assumed to be the net stress exhibited by the lattice nodes, which does not account for any stress concentration effect of the lattice nodes. Table 6 reports the ratio $\frac{A_g}{A_{g,hom}}$ between the net section on the lattice nodes, A_g, and cross section of the homogeneous material associated to the lattice structure at the apparent macroscopic scale, $A_{g,hom}$, for the analyzed BCC and D samples.

Table 5
Experimental data used for the validation of the multiaxial ALM model (Eqs. (7)–(10)).

$\Delta\overline{w}_{th} = 0.204$ MPa	Estimated using Eq. (11), where: $\Delta\sigma_0 = 155.0$ MPa at $R = 0.1$, determined using Eq. (13), where: σ_{UTS} is experimentally measured, Fig. 10, and the calibration constant is set to 1; $E = 72\,000$ MPa; $c_w = 1.222$.
$R_c = 0.050$ mm	Estimated using Eq. (12), where: $e_1 = 0.125$, $c_w = 1.222$; $\Delta K_{th,LC} = 2.2$ MPa $m^{0.5}$, experimentally measured at $R = 0.1$, Fig. 11.

Fig. 18 presents the FE model used to estimate the N-SIFs, in which (i) the lattice nodes are modeled as a pointed V-notch (i.e., with a zero notch tip radius), and (ii) each strut is modeled as a straight cylinder with diameter d as reported in Table 6. The nominal strut diameter in the CAD model was iteratively adjusted in increments of 10 μm until the mass of the virtual lattice specimen matched the experimentally measured mass of the corresponding additively manufactured sample. The resulting diameter was then adopted in the FE model, in accordance with standard practice (e.g., [25,55]). Consequently, manufacturing defects and geometry discrepancies (e.g., strut waviness, surface roughness, or internal porosity) were neglected.

The FE analyses were performed in Ansys® Mechanical 2024 r2 by adopting 3D, 10-node tetrahedral elements with quadratic formulation (SOLID 187 from the ANSYS® library). The FE mesh was generated with the free meshing algorithm, using a nominal element size of 0.5 mm on all volumes and 0.05 mm on all V-notch tip lines; transition from the fine to coarse FE mesh pattern was arranged by using a growth rate of 1.2. Note that the selected FE mesh size is finer than suggested in [27,28] for the applicability of the PSM; on the other hand, this refined FE mesh enabled the evaluation of relatively large SIF values along each entire notch tip line.

The FE model results are reported in Fig. 19 in terms of the averaged SED along the V-notch tip line under an applied remote stress $\sigma_{g,hom}$ = 1 MPa for both BCC and D samples; the averaged SED was computed

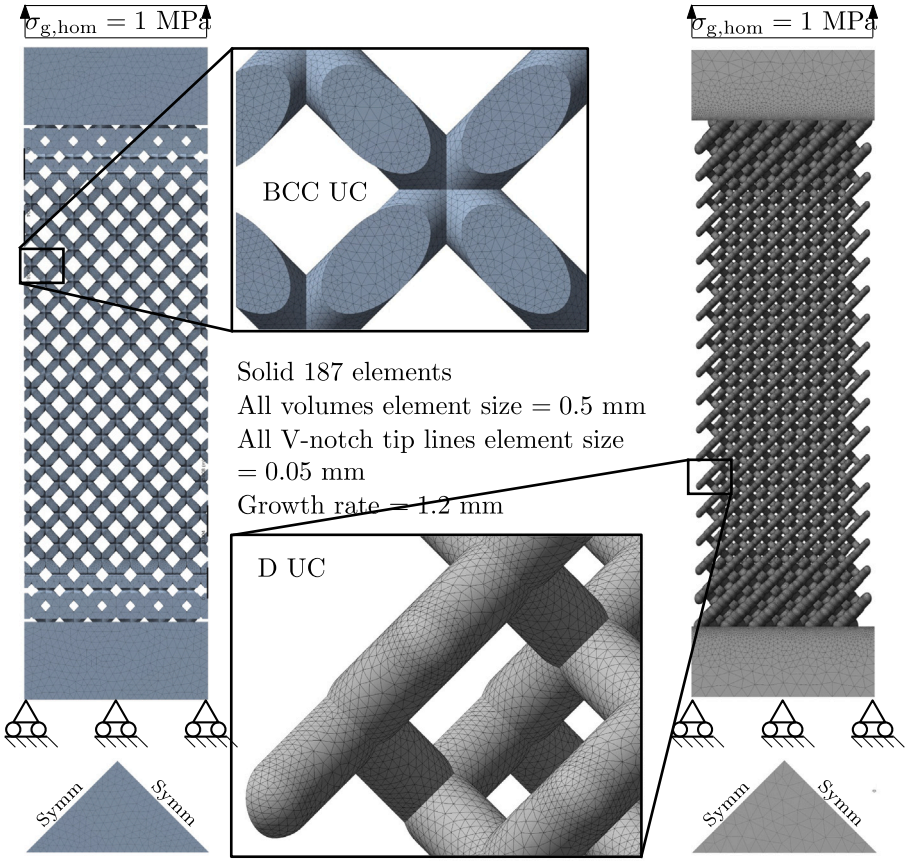

Fig. 18. Schematic FE model description for the BCC (on the left) and D (on the right) lattice samples analyzed in the present investigation.

according to Eq. (5). The node identified as most critical by the FE analyses is highlighted in Fig. 19 by the red inset. At the unit cell scale, the numerical results are consistent with the fractographic analysis (Fig. 16) for both UCs. At the specimen scale, the FE analyses locate the most critical node within the gauge section, in agreement with the observed failure location. However, since the experimental setup did not allow in situ monitoring of individual nodes during fatigue testing, a direct one-to-one correspondence between the numerically identified critical node and the experimentally failed node cannot be established.

The effective crack sizes for each local stress mode, $a_{\mathrm{eff,i}}$, the equivalent threshold SIF, $\Delta K^{\mathrm{v}}_{\mathrm{eq}\Delta\bar{w},\mathrm{th}}$, the equivalent El-Haddad material parameter, $a^{\mathrm{v}}_{0,\mathrm{eq}\Delta\bar{w}}$, the equivalent V-notch size, $a^{\mathrm{v}}_{\mathrm{eq}\Delta\bar{w}}$, and the theoretical and experimental fatigue limits for each lattice structure are reported in Table 6 for the most critical node (Fig. 19). The experimental fatigue limits reported in Figs. 14 and 15 and the theoretical fatigue limits reported in Table 6 are compared in the ALM diagram reported in Fig. 20.

Table 6 and Fig. 20 show satisfactory agreement between theoretical and experimental fatigue limits, with discrepancies below 10%. It is worth noting that:

1. for both UCs analyzed, the obtained values of $a^{\mathrm{v}}_{\mathrm{eq}\Delta\bar{w}}$ are significantly larger than $a^{\mathrm{v}}_{0,\mathrm{eq}\Delta\bar{w}}$, Fig. 20, confirming the long and sharp notch behavior of the lattice nodes analyzed in the present investigation. Consequently, similar results would be obtained even if the contribution of $a^{\mathrm{v}}_{0,\mathrm{eq}\Delta\bar{w}}$ were neglected in Eqs. (7)–(10), and the fatigue limit estimations are therefore only weakly influenced by the estimation of $\Delta\sigma_0$ for m values between 0.8 and 1 in Eq. (13);
2. the BCC samples are subjected only to mode 1 local stresses, mode 3 local stresses being negligible as demonstrated by: (i) the far lower value of a_{eff_3} compared to a_{eff_1}, and (ii) the ratio of the SED contribution due to mode 1 and mode 3 local stresses reported in Table 6. As a consequence, Eqs. (7)–(10) practically simplify to the previously published uniaxial ALM model for V-notches, Eq. (4).
3. the D specimens are subjected to local multiaxial stresses, with both mode 1 and mode 3 components being present. However, the contribution of mode 3 is approximately one order of magnitude lower than that of mode 1 ($\Delta\bar{w}_1/\Delta\bar{w}_3$). Therefore, given the limited contribution of mode 3 local stresses, the use of a single structural radius calibrated on mode 1 local stresses (i.e., $R_c = R_1$) is not expected to significantly affect the results. This assumption is further supported by the fact that the structural radii associated with mode 2 and mode 3 local stress singularities are generally larger than that associated with mode 1, as discussed elsewhere [30].
4. for both UCs analyzed, the approximate estimation of the plastic zone size is significantly smaller than the corresponding effective crack size, indicating that the region governing the fatigue behavior is dominated by linear elastic stress fields. This circumstance supports the use of the LEFM-based approach adopted in the present work.

6. Discussions

An alternative approach to analyze the short crack effect of the ALM diagram was proposed by Lazzarin and Berto [20]. When extended to V-notches, it consists in estimating the fatigue limit of the notched structure using the averaged SED model by scaling the size of the sample in geometrical similitude, while keeping the structural volume size constant because it is a material–microstructure–environment property. Lazzarin and Berto showed that for the simple geometries analyzed

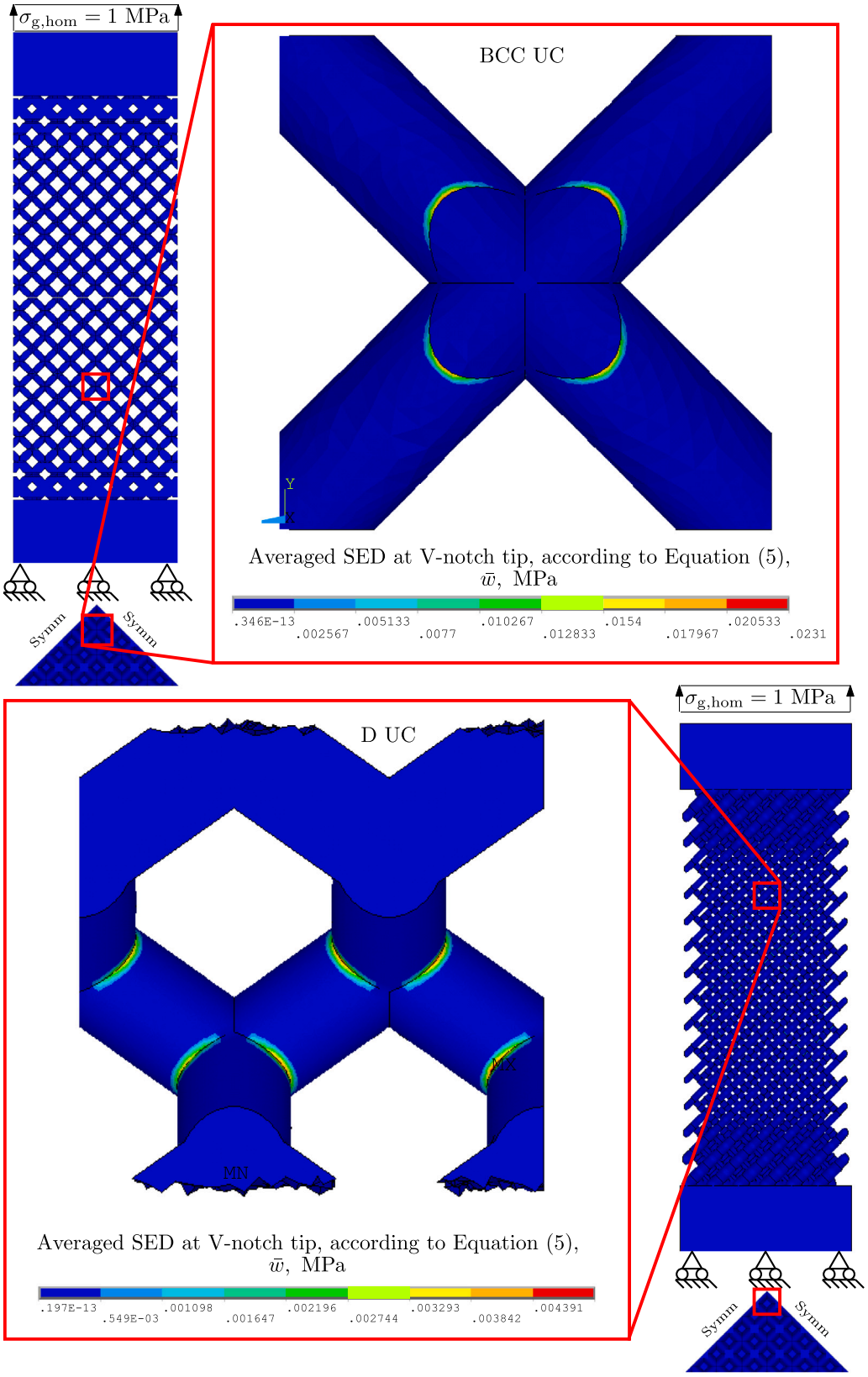

Fig. 19. Distribution of the averaged Strain Energy Density (SED) along the notch tip line for the BCC (top) and Diamond (bottom) lattice structures under a reference remote stress $\sigma_{ghom} = 1$ MPa; the SED is computed within the structural volume according to Eq. (5); the most critical node is highlighted by the red inset.

Table 6
Comparison between experimental and theoretical fatigue thresholds of lattice specimens according to the ALM model; the material properties are reported in Table 5.

Type	d_{AB} (mm)	2α (°deg)	γ_1	γ_3	e_1	e_3	$a_{eff,1}$ (mm)	$a_{eff,3}$ (mm)	$\Delta K^{v}_{eq\Delta\bar{w},th}$ (MPa mm$^{\gamma}$)	$a^{v}_{0,eq\Delta\bar{w}}$ (mm$^{\gamma}$)	$a^{v}_{eq\Delta\bar{w}}$ (mm$^{\gamma}$)
BCC	0.55	71	0.48	0.38	0.14	0.20	3.0	3.7e−5	8.4	9.4e−4	4.3e−2
D	0.52	109	0.41	0.28	0.13	0.29	4.3	1.6e−1	14	2.5e−3	9.0e−2

Type	$\Delta\sigma^{exp}_{g,hom,th}$ (MPa)	$\Delta\sigma^{est}_{g,hom,th}$ (MPa)	$\frac{A_g}{A_{g,hom}}$ (%)	$\Delta\sigma_0$♠ (MPa)	$\Delta\bar{w}_{th}$♠ (MPa)	R_c♠ (mm)	$\Delta\bar{w}_1/\Delta\bar{w}_3$◇	Plastic size♣ (mm)
BCC	2.8	2.6	11.7	155	0.204	0.050	>1e4	0.042
D	5.4	5.8	22.2	155	0.204	0.050	≃10	0.043

d_{AB}: is the as built strut diameter, determined by matching the mass of the small representative specimens to that of the CAD model in the test section, following standard practice (e.g., [25,55]).
2α: is the notch opening angle, determined from the FE model using the automated PSM procedure [29].
$a_{eff,\gamma}$: is null for both lattice series of lattice samples at the most critical location.
$\Delta\sigma^{exp}_{g,hom,th}$: Experimental fatigue limit referred to the homogeneous material associated to the lattice structure at the apparent macroscopic scale, determined with the short staircase sequence and reported in Figs. 14, 15.
$\Delta\sigma^{est}_{g,hom,th}$: Estimated fatigue limit referred to the homogeneous material associated to the lattice structure at the apparent macroscopic scale using the ALM model, Eqs. (7)–(10).
♠: Values taken from Table 5.
◇: ratio between the averaged SED contribution due to mode 1 local stresses over the contribution due to mode 3 local stresses computed with Eq. (5).
Plastic size♣: simplified estimation of the plastic zone size, defined as the distance from the notch tip at which the local opening stress achieves the monotonic quasi-static yield strength. It is evaluated at the maximum value of the mode 1 N-SIF at the estimated fatigue limit as:
Plastic size $= \left[\left(\frac{\Delta K^{v}_{1,th}}{1-R}\right) / \left(\sqrt{2\pi}\sigma_Y\right)\right]^{(1/\gamma_1)} \rightarrow = \left[\left(\frac{\Delta\sigma^{est}_{g,hom,th}\cdot a^{\gamma_1}_{eff,1}}{1-R}\cdot\frac{A_{g,hom}}{A_g}\right) / \left(\sqrt{2}\sigma_Y\right)\right]^{(1/\gamma_1)}$.

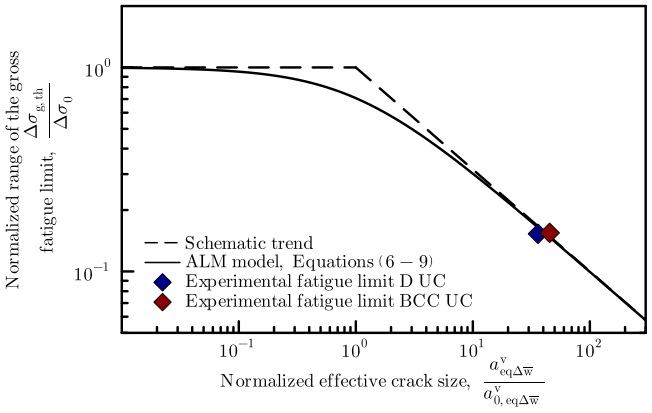

Fig. 20. Comparison between ALM model, Eqs. (7)–(10), and experimental fatigue limits, where σ_g is the net stress exhibited by the lattice nodes; the ratio between A_g and the cross section of the homogeneous material at the apparent macroscopic scale, $A_{g,hom}$ is reported in Table 6.

in [20] (cracks, U- and V-notches centered in an infinite plate subjected to pure mode 1 local stresses due to remote tension), the SED-based fatigue limit estimation leads to the same results of the ALM model, Eq. (4), and the same results of the well known Kitagawa diagram in the case of cracks. According to the interpretation given by Lazzarin and Berto [20], the defect and notch sensitivities can be attributed to the presence of higher order terms in the structural volume, as discussed in Section 2. In this context the present authors point out that:

- the averaged SED does not explicitly provide a physical explanation of the defect and notch sensitivity behavior; as an example it does not include in its formulation crack closure phenomena, which are known to play an important role in building the defect sensitivity phenomena;
- similarly to the ALM model, the averaged SED requires two material parameters for its calibration: $\Delta\bar{w}_{th}$ and R_c. Interestingly, both parameters can be determined using the same material properties required to calibrate the ALM model, Eqs. (11) and (12), highlighting once again the intimate relationship between the two approaches.

Fig. 21 shows the ALM diagram for both the BCC and D lattice structures adopting the framework proposed by Berto and Lazzarin described above. It plots the strut diameter on the x-axis and the fatigue limit on the y-axis, where the nominal stress is referred to the homogenized material associated to the lattice structure at the macroscopic scale. The fatigue limits are reported with cross markers in Fig. 21 and have been estimated as:

$$\Delta\sigma_{g,th} = \sqrt{\frac{\Delta\bar{w}_{th}}{\Delta\bar{w}}}\cdot\Delta\sigma_g, \tag{17}$$

for each strut diameter analyzed, where $\Delta\bar{w}_{th}$ is reported in Table 5; $\Delta\bar{w}$ is estimated by calculating the SED in the structural volume for a remote stress of $\sigma_{g,hom} = 1$ MPa, corrected for the remote force ratio using the proper $c_w = 1.222$ (i.e. $\Delta\bar{w} = \bar{w}_{1\ MPa}\cdot c_w$, $\bar{w}_{1\ MPa}$ being the averaged SED obtained from FE simulation with a 1 MPa remote tension applied, as shown in Fig. 18).

The structural volume was defined as a cylindrical sector parallel to the notch bisector of radius R_c as reported in Table 5 and thickness of 2 μm, which was located at the critical node estimated using the PSM and Eqs. (7)–(10). The adopted FE mesh size in the structural volume was 1 μm. The reduced thickness ensures that the structural volume captured only the stress gradient along the notch bisector, thereby complying to the definition of a structural volume of unit thickness.

The smallest strut size analyzed corresponds to the geometrical condition where the two structural volumes centered at opposite V-notch tips of the same lattice node are tangent (this geometrical condition is approximately when the structural volume radius equals the strut radius). If the strut size was further reduced, the two opposite structural volumes would start to overlap. This situation was discussed by Lazzarin and Berto [20], but is not further explored in this work, as Fig. 21 clarifies that the UC sizes of the BCC and D samples are well larger than the size which produces tangency of the opposite structural volumes.

For the BCC sample, the SED-determined ALM diagram (Fig. 21) shows a trend related to the defect sensitivity behavior that differs from the ALM model, Fig. 20. This trend can be explained by analyzing the stress field distribution around the notches, as shown in Fig. 22. It shows that due to the presence of bending stresses that arise from the bending-dominated nature of the BCC structure, the first order approximation, on which the ALM model is based, leads to an overestimation

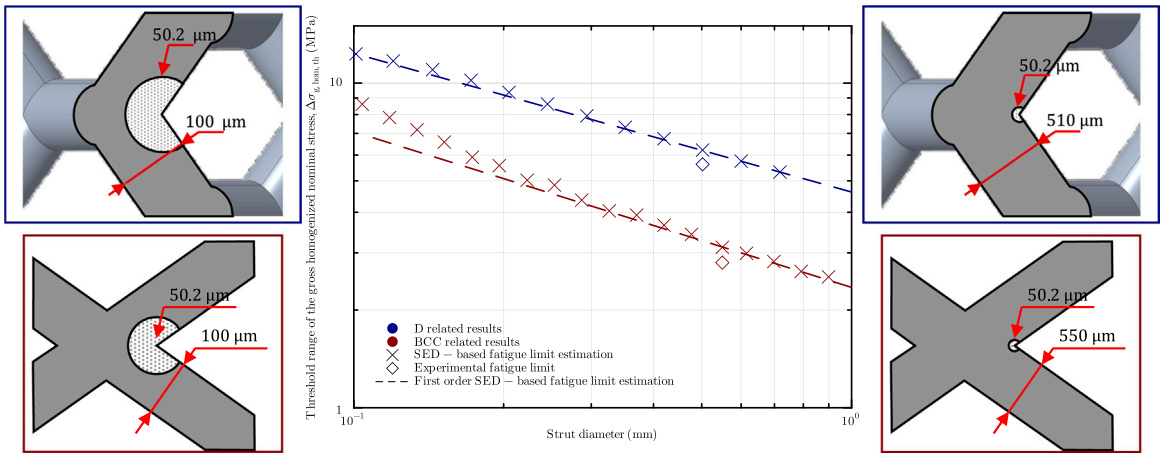

Fig. 21. SED-based ALM diagram for the BCC and D samples.

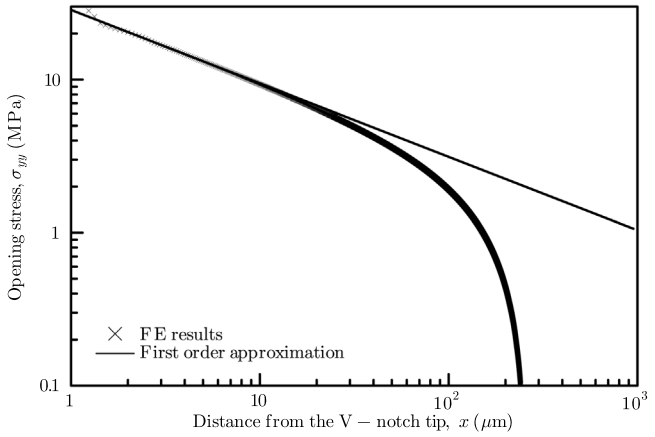

Fig. 22. Stress field distribution along the V-notch bisector for the BCC samples with strut diameter of 0.55 mm.

of the stress field magnitude when progressively moving away from the notch tip. As a consequence, as soon as higher order terms become relevant in the structural volume, the averaged SED decreases more rapidly than expected with the first order approximation, leading to the peculiar defect sensitivity-like behavior observed in Fig. 21.

For the D sample, the SED-determined ALM diagram aligns more closely with the ALM model, and the defect sensitivity behavior is never achieved, even for the smallest strut sizes analyzed, likely because of the lesser extent of bending dominated stresses.

6.1. Applicability limits of the sharp-notch assumption for lattice structures

The present authors observe that the sharp V-notch behavior, which prevails over the influence of AM defects in the competition for fatigue failure in the present investigation, cannot be assumed valid for any lattice structure. In general, this assumption must be re-evaluated for each specific application, at least by analyzing the scatter of the $\Delta\sigma_g - N_f$ curves and the fatigue fracture surfaces, according to the suggestions made in the present investigation.

Blunt notch behavior is expected in shell-based lattice structures, where severe stress concentrators are not present. In such cases, fatigue cracks are typically initiated by individual defects or clusters of defects; these cracks subsequently coalesce into a dominant crack, progressively leading to fatigue failure. A notable example is represented by the TPMS (Triply Periodic Minimal Surface) lattice structures tested by Gavazzoni et al. in [22], in which defects were shown to govern crack initiation. Under these conditions, the fundamental assumption of notch-driven fatigue is no longer valid. Therefore, a defect-tolerant approach is more appropriate, as extensively discussed in the literature [6].

6.2. Outlook for future research

The present study highlights several directions for future investigation:

- assessing the consistency between the microstructure of the bulk specimens and that of the lattice structures deserves further investigation. LEFM-based approaches rely on the implicit assumption that the material properties adopted for fatigue limit estimation are consistent with those used for calibration. In the present analysis, the stress-relief heat treatment likely promoted microstructural homogenization;
- the estimation of the fatigue limit of the defect-free material associated to AMed parts is not straightforward, since defects are inevitably present. Consequently, $\Delta\sigma_0$ cannot be determined experimentally by performing fatigue tests on plain specimens, and indirect methods relating the fatigue limit to other, less defect-sensitive, mechanical properties must be adopted. The most common approaches in the literature are correlations with the ultimate tensile strength (as done in the present work, $\Delta\sigma_0\,(R=-1) = \sigma_{UTS}$) and with the Vickers hardness ($\Delta\sigma_0\,(R=-1) = 1.6 \cdot HV$, [56]). Further research on this topic would be desirable to reduce the uncertainty associated with the calibration of LEFM-based fatigue strength models;
- a more detailed metrological characterization would improve the accuracy of the local stress field estimation. This should not be limited to the strut diameter calibration performed in the present work, but should also include, surface roughness, fillet radii at the lattice nodes, and non-circular cross sections of the beams. Such improvements, combined with refined FE analyses, would further enhance the accuracy of the local stress field estimation;
- the adoption of local damage monitoring techniques would enable the investigation of crack initiation and propagation at the level of individual struts, overcoming the limitations associated with using complete specimen failure as the sole failure criterion. Notable examples are reported in [26], where fatigue tests were conducted inside a μX-CT scanner to monitor the evolution of damage during fatigue loading;
- the present study focuses on the fatigue limit estimation of AMed lattice structures using non-conventional extensions of LEFM. This specific condition is relevant for several engineering applications, where maintenance is complex. However, local stress field

approaches have also proven effective for fatigue strength estimation in the finite life regime, typically in the range 10^4–10^6 cycles, in several engineering applications such as weldments [28].

According to the present authors, the fatigue strength of AMed lattice structures can be estimated using the same methods discussed in this work also in the finite life regime (and, if properly calibrated, in the very high-cycle fatigue regime). However, being based on the initial stress field distribution, such approaches inherently neglect stress redistribution due to crack propagation and are therefore expected to be mainly applicable to crack initiation life rather than to complete failure. This circumstance is particularly relevant for lattice structures, where the intricate geometry is likely to result in a significant contribution of crack propagation to the total fatigue life.

7. Conclusions

This study discussed the fatigue strength of lattice structures, considering them as defective and notched structures rather than analyzing them with a homogenized approach. The findings have shown that the fatigue limit of lattice structures can be estimated using the Atzori–Lazzarin–Meneghetti (ALM) model according to the recent multiaxial formulation [30], which allows estimating the fatigue limit for any defect, crack or sharp U- and V-notch and any local stress field, including multiaxiality from the properties of the base material.

The ALM-based fatigue limit estimation was validated against experimental results relevant to two lattice structures with Body Centered Cubic (BCC) and Diamond (D) Unit Cells (UCs), respectively, which were manufactured via Laser Powder Bed Fusion (L-PBF) of aluminium A205 powder.

The main conclusions that can be drawn from the investigation are:

- the application of the multi-contour scanning strategy together with the dedicated process parameter optimization proposed by Beevers et al. [35] allowed for the fabrication of nearly defect-free lattice structures. This was evidenced by the high relative density of the samples and the absence of fatigue crack initiation from internal porosities, which instead initiated from the sharp V-shaped notches at the lattice nodes;
- the experimental setup and specimen geometry adopted in the present work enabled the characterization of the fatigue strength of lattice structures and provided insights into fatigue crack initiation mechanisms through fracture surface analysis;
- as a result of the fatigue tests and fracture surface analysis of the broken specimens, the lattice structures behaved as sharp V-shaped notches, which was highlighted by: (i) the reduced scatter, especially for the diamond UC, and (ii) the presence of multiple crack initiations along the V-notch tip line at the lattice nodes and the lack of defects on the fatigue fracture surfaces.

Comparing the experimental results with the fatigue limit estimations based on the multiaxial ALM model showed satisfactory agreement, with discrepancies below 10% for both lattice structures analyzed.

The outcome of the present investigation being valid, lattice structures do not necessarily behave like sharp V-notches; instead, generally speaking lattice structures are notched and defective materials, where local stress field approaches enable to manage the competition for fatigue failure between defects and notches.

CRediT authorship contribution statement

Francesco Collini: Writing – review & editing, Writing – original draft, Visualization, Validation, Software, Methodology, Investigation, Formal analysis, Data curation, Conceptualization. **Berk Baris Celik:** Writing – review & editing, Validation, Investigation. **Emilie Beevers:** Writing – review & editing, Validation, Investigation. **Brecht Van Hooreweder:** Writing – review & editing, Validation, Investigation. **Giovanni Meneghetti:** Writing – review & editing, Visualization, Validation, Supervision, Resources, Project administration, Methodology, Investigation, Funding acquisition, Formal analysis, Conceptualization.

Declaration of competing interest

The authors declare that they have no known competing financial interests or personal relationships that could have appeared to influence the work reported in this paper.

Acknowledgments

This study was carried out within the MICS (Made in Italy - Circular and Sustainable) Extended Partnership and received funding from the European Union Next-Generation EU (PIANO NAZIONALE DI RIPRESA E RESILIENZA (PNRR)-MISSIONE 4 COMPONENTE 2, INVESTIMENTO 1.3- D.D. 1551.11-10-2022, PE00000004). This manuscript reflects only the authors' views and opinions, neither the European Union nor the European Commission can be considered responsible for them.

The present authors would like to acknowledge Filippo Coppola (University of Padua, Department of Industrial Engineering) for support in the SEM analyses of the microstructural characterization and Alberto Visentin (University of Padua, Department of Industrial Engineering) for support in the automatization of the finite element analyses.

Data availability

Data will be made available on request.

References

[1] Inventory of U.S. greenhouse gas emissions and sinks: 1990–2017. U.S. Environmental Protection Agency.
[2] du Plessis A, Razavi SMJ, Benedetti M, Murchio S, Leary M, Watson M, Bhate D, Berto F. Properties and applications of additively manufactured metallic cellular materials: A review. Prog Mater Sci 2022;125:100918. http://dx.doi.org/10.1016/j.pmatsci.2021.100918.
[3] Benedetti M, du Plessis A, Ritchie RO, Dallago M, Razavi SM, Berto F. Architected cellular materials: A review on their mechanical properties towards fatigue-tolerant design and fabrication. Mater Sci Eng: R: Rep 2021;144:100606. http://dx.doi.org/10.1016/J.MSER.2021.100606.
[4] Ghidini T, Grasso M, Gumpinger J, Makaya A, Colosimo B. Additive manufacturing in the new space economy: Current achievements and future perspectives. Prog Aerosp Sci 2023;142:100959. http://dx.doi.org/10.1016/j.paerosci.2023.100959.
[5] Ashby MF. The properties of foams and lattices. Philos Trans R Soc A 2005;364:15–30. http://dx.doi.org/10.1098/RSTA.2005.1678.
[6] Collini F, Meneghetti G. Towards a fracture mechanics-based fatigue assessment of lattice structures obtained from additive manufacturing of metallic powders. Mater Des 2024;244:113077. http://dx.doi.org/10.1016/j.matdes.2024.113077.
[7] Dunne F, Wilkinson A, Allen R. Experimental and computational studies of low cycle fatigue crack nucleation in a polycrystal. Int J Plast 2007;23(2):273–95.
[8] McDowell D, Dunne F. Microstructure-sensitive computational modeling of fatigue crack formation. Int J Fatigue 2010;32(9):1521–42.
[9] Sangid MD. The physics of fatigue crack initiation. Int J Fatigue 2013;57:58–72. http://dx.doi.org/10.1016/J.IJFATIGUE.2012.10.009.
[10] Neuber H. Theory of notch stresses. Berlin: Springer-Verlag; 1958.
[11] Taylor D. The theory of critical distances. Eng Fract Mech 2008;75(7):1696–705.
[12] Susmel L. Multiaxial notch fatigue. Elsevier; 2009.
[13] Susmel L, Taylor D. A critical distance/plane method to estimate finite life of notched components under variable amplitude uniaxial/multiaxial fatigue loading. Int J Fatigue 2012;38:7–24.
[14] Susmel L. Four stress analysis strategies to use the modified Wöhler curve method to perform the fatigue assessment of weldments subjected to constant and variable amplitude multiaxial fatigue loading. Int J Fatigue 2014;67:38–54.
[15] Kouanga CT, Nowell D, Joyce RD, Susmel L. Critical plane and critical distance approaches to assess damage under variable amplitude fretting fatigue loading. In: Fracture, fatigue and wear. Springer; 2021, p. 161–73.

[16] Susmel L, Taylor D. The modified Wöhler curve method applied along with the theory of critical distances to estimate finite life of notched components subjected to complex multiaxial loading paths. Fatigue Fract Eng Mater Struct 2008;31(12):1047–64. http://dx.doi.org/10.1111/j.1460-2695.2008.01296.x.
[17] Naik RA, Lanning DB, Nicholas T, Kallmeyer AR. A critical plane gradient approach for the prediction of notched HCF life. Int J Fatigue 2005;27(5):481–92.
[18] Carpinteri A, Spagnoli A, Vantadori S, Viappiani D. A multiaxial criterion for notch high-cycle fatigue using a critical-point method. Eng Fract Mech 2008;75(7):1864–74.
[19] Lazzarin P, Zambardi R. A finite-volume-energy based approach to predict the static and fatigue behavior of components with sharp V-shaped notches. Int J Fract 2001 112:3 2001;112:275–98. http://dx.doi.org/10.1023/A:1013595930617.
[20] Lazzarin P, Berto F. From Neuber's elementary volume to Kitagawa and Atzori's diagrams: an interpretation based on local energy. Int J Fract 2005;135:L33–8.
[21] Boniotti L, Beretta S, Patriarca L, Rigoni L, Foletti S. Experimental and numerical investigation on compressive fatigue strength of lattice structures of AlSi7Mg manufactured by SLM. Int J Fatigue 2019;128:105181. http://dx.doi.org/10.1016/J.IJFATIGUE.2019.06.041.
[22] Gavazzoni M, Beretta S, Foletti S. Response of an aluminium Schwarz triply periodic minimal surface lattice structure under constant amplitude and random fatigue. Int J Fatigue 2022;163:107020. http://dx.doi.org/10.1016/j.ijfatigue.2022.107020.
[23] Raghavendra S, Dallago M, Zanini F, Carmignato S, Berto F, Benedetti M. A probabilistic average strain energy density approach to assess the fatigue strength of additively manufactured cellular lattice materials. Int J Fatigue 2023;172:107601. http://dx.doi.org/10.1016/J.IJFATIGUE.2023.107601.
[24] De Biasi R, Oztoprak O, Zanini F, Carmignato S, Kollmannsberger S, Benedetti M. Predicting fatigue life of additively manufactured lattice structures using the image-based finite cell method and average strain energy density. Mater Des 2024;246:113321. http://dx.doi.org/10.1016/j.matdes.2024.113321.
[25] Pelegatti M, Benasciutti D, De Bona F, Salvati E. Low cycle fatigue modelling of cellular materials produced by laser-powder bed fusion. Mater Des 2024;244:113201. http://dx.doi.org/10.1016/j.matdes.2024.113201.
[26] Boniotti L, Dancette S, Gavazzoni M, Lachambre J, Buffiere JY, Foletti S. Experimental and numerical investigation on fatigue damage in micro-lattice materials by digital volume correlation and μCT-based finite element models. Eng Fract Mech 2022;266:108370. http://dx.doi.org/10.1016/J.ENGFRACMECH.2022.108370.
[27] Meneghetti G, Lazzarin P. Significance of the elastic peak stress evaluated by FE analyses at the point of singularity of sharp V-notched components. Fatigue Fract Eng Mater Struct 2007;30:95–106. http://dx.doi.org/10.1111/j.1460-2695.2006.01084.x.
[28] Meneghetti G, Campagnolo A. State-of-the-art review of peak stress method for fatigue strength assessment of welded joints. Int J Fatigue 2020;139:105705. http://dx.doi.org/10.1016/j.ijfatigue.2020.105705.
[29] Visentin A, Campagnolo A, Babini V, Meneghetti G. Automated implementation of the peak stress method for the fatigue assessment of complex welded structures. Forces Mech 2022;6:100072. http://dx.doi.org/10.1016/j.finmec.2022.100072.
[30] Collini F, Rigon D, Meneghetti G. Notch and fracture mechanics-based assessment of multiaxial fatigue thresholds of defects and sharp notches in metallic materials. Fatigue Fract Eng Mater Struct 2025;48(4):1929–70. http://dx.doi.org/10.1111/ffe.14478.
[31] Rigon D, Meneghetti G. An engineering estimation of fatigue thresholds from a microstructural size and Vickers hardness: application to wrought and additively manufactured metals. Int J Fatigue 2020;139. http://dx.doi.org/10.1016/J.IJFATIGUE.2020.105796.
[32] Rigon D, Coppola F, Meneghetti G. Fracture mechanics-based analysis of the fatigue limit of Ti6Al4V alloy specimens manufactured by SLM in as-built surface conditions by means of areal measurements. Eng Fract Mech 2024;295:109720. http://dx.doi.org/10.1016/j.engfracmech.2023.109720.
[33] Meneghetti G, Rigon D, Gennari C. An analysis of defects influence on axial fatigue strength of maraging steel specimens produced by additive manufacturing. Int J Fatigue 2019;118:54–64. http://dx.doi.org/10.1016/J.IJFATIGUE.2018.08.034.
[34] Collini F, Meneghetti G. Fracture and notch mechanics to estimate the uniaxial fatigue limit of plain and severely notched L-PBF AlSi10Mg specimens. Eng Fract Mech 2025;326:111368. http://dx.doi.org/10.1016/j.engfracmech.2025.111368.
[35] Beevers E, Cutolo A, Van Hooreweder B. Finetuning design and process conditions to minimise manufacturing deviations in strut-based metal lattice structures produced by laser powder bed fusion. Appl Mater Today 2025;42:102551. http://dx.doi.org/10.1016/j.apmt.2024.102551.
[36] Atzori B, Lazzarin P. Notch sensitivity and defect sensitivity under fatigue loading: Two sides of the same medal. Int J Fract 2001;107:1–8. http://dx.doi.org/10.1023/A:1007686727207.
[37] Atzori B, Lazzarin P, Meneghetti G. Fracture mechanics and notch sensitivity. Fatigue Fract Eng Mater Struct 2003;26:257–67. http://dx.doi.org/10.1046/J.1460-2695.2003.00633.X.
[38] Atzori B, Lazzarin P, Meneghetti G. A unified treatment of the mode I fatigue limit of components containing notches or defects. Int J Fract 2005 133:1 2005;133:61–87. http://dx.doi.org/10.1007/S10704-005-2183-0.
[39] Williams ML. Stress singularities resulting from various boundary conditions in angular corners of plates in extension. 1952.
[40] Gross B, Mendelson A. Plane elastostatic analysis of V-notched plates. Int J Fract Mech 1972;8:267–76.
[41] Lazzarin P, Tovo R. A unified approach to the evaluation of linear elastic stress fields in the neighborhood of cracks and notches. Int J Fract 1996 78:1 1996;78:3–19. http://dx.doi.org/10.1007/BF00018497.
[42] Lazzarin P, Filippi S. A generalized stress intensity factor to be applied to rounded V-shaped notches. Int J Solids Struct 2006;43(9):2461–78.
[43] Atzori B, Meneghetti G. Notch and defect sensitivity of ADI in torsional fatigue. In: Fracture of nano and engineering materials and structures: proceedings of the 16th European conference of fracture, Alexandroupolis, Greece, July 3–7, 2006. Springer; 2006, p. 201–2.
[44] Haddad MHE, Smith KN, Topper TH. Fatigue crack propagation of short cracks. J Eng Mater Technol 1979;101:42–6. http://dx.doi.org/10.1115/1.3443647.
[45] Haddad MHE, Topper TH, Smith KN. Prediction of non propagating cracks. Eng Fract Mech 1979;11:573–84. http://dx.doi.org/10.1016/0013-7944(79)90081-X.
[46] Neuber H. Über die berücksichtigung der spannungskonzentration bei festigkeitsberechnungen. Konstruktion 1986;245–51.
[47] Lazzarin P, Sonsino CM, Zambardi R. A notch stress intensity approach to assess the multiaxial fatigue strength of welded tube-to-flange joints subjected to combined loadings. Fatigue Fract Eng Mater Struct 2004;27(2):127–40. http://dx.doi.org/10.1111/j.1460-2695.2004.00733.x.
[48] Berto F, Lazzarin P, Yates JR. Multiaxial fatigue of V-notched steel specimens: a non-conventional application of the local energy method. Fatigue Fract Eng Mater Struct 2011;34:921–43. http://dx.doi.org/10.1111/j.1460-2695.2011.01585.x.
[49] Atzori B, Berto F, Lazzarin P, Quaresimin M. Multi-axial fatigue behaviour of a severely notched carbon steel. Int J Fatigue 2006;28(5–6):485–93.
[50] Dowling NE. Mechanical behavior of materials. Engineering methods for deformation, fracture, and fatigue. Pearson; 2013.
[51] Goodman J. Mechanics applied to engineering. London, UK: Longmans Green; 1899.
[52] A. m. t. Ltd. Materials data sheet a205 gas atomised powder. 2020.
[53] Maamoun AH, Elbestawi M, Dosbaeva GK, Veldhuis SC. Thermal post-processing of AlSi10Mg parts produced by selective laser melting using recycled powder. Addit Manuf 2018;21:234–47. http://dx.doi.org/10.1016/j.addma.2018.03.014.
[54] Dixon WJ. The up-and-down method for small samples. J Amer Statist Assoc 1965;60:967–78. http://dx.doi.org/10.1080/01621459.1965.10480843.
[55] Van Hooreweder B, Apers Y, Lietaert K, Kruth JP. Improving the fatigue performance of porous metallic biomaterials produced by Selective Laser Melting. Acta Biomater 2017;47:193–202. http://dx.doi.org/10.1016/J.ACTBIO.2016.10.005.
[56] Murakami Y. Metal fatigue: Effects of small defects and nonmetallic inclusions.